Australian Government
Department of Defence
Defence Science and
Technology Organisation

High Grazing Angle and High Resolution Sea Clutter: Correlation and Polarisation Analyses

Yunhan Dong

Electronic Warfare and Radar Division
Defence Science and Technology Organisation

DSTO-TR-1972

ABSTRACT

Spatial and temporal correlations of high grazing angle high resolution sea clutter collected by the DSTO Ingara polarimetric X-band system are studied. It seems that wavelengths of wind waves and swells are retrievable from the range correlation whereas the periods of the waves and swells are recoverable from the azimuthal correlation. The polarimetric behaviour of sea clutter is also studied, and it is found that the Bragg scattering is the dominant scattering mechanism of the sea clutter. Quantitative analysis indicates that the best polarisations in terms of detecting small targets on the sea surface include double bounce, cross-slant-45-degree, RR and HH polarisations.

RELEASE LIMITATION

Approved for public release

Published by

Defence Science and Technology Organisation
PO Box 1500
Edinburgh South Australia 5111   Australia

Telephone: (08) 8259 5555
Fax: (08) 8259 6567

AR-013-872
March 2007

APPROVED FOR PUBLIC RELEASE

High Grazing Angle and High Resolution Sea Clutter: Correlation and Polarisation Analyses

Executive Summary (U)

This report contributes to the delivery of *Milestone 4.1.1.1.1: High grazing angle sea clutter and target signatures* in the AIR 7000 S&T Plan (Annex C – Technical Support Plan). The outcomes of the analysis contained herein will also form a component of the model delivered for *Milestone 4.1.1.1.2: Radar modelling capability development – maritime* of the Technical Support Plan. These activities are aimed at better understanding of the radar performance drivers for operation of High Altitude Long Endurance (HALE) unmanned aerial vehicles (UAVs) in the maritime surveillance role, and therefore reducing risk in any acquisition decision.

The nature and characteristics of sea clutter depend on both sea conditions and radar parameters. Extensive studies of sea clutter have been reported in the literature in the last few decades. Most of these studies, however, are based on sea clutter collected at low grazing angles. The grazing angle in these studies ranges from zero to several degrees, a typical configuration for applications of radars on ship or at coast. Maritime patrol aircraft views the sea surface at much higher grazing angles than ship or land observatory. Since the dominant scattering mechanisms in sea clutter at low and high grazing angles are different, it would not be surprising if the nature and characteristics of the corresponding sea clutter are also different.

DSTO conducted a Sea Clutter Trial in 2004 (SCT04) in the Southern Ocean at a location approximately 100 km south of Port Lincoln in South Australia. Sea clutter data was collected in the trial using the DSTO developed X-band polarimetric airborne radar system (known as Ingara system). Details of the trial and sea clutter analysis have been reported elsewhere (Crisp et al, DSTO-TR-18182006).

A previous report has studied the statistical distribution of high grazing angle sea clutter from SCT04 DSTO-RR-0136. Models better than the traditional K- or Weibull distributions, aimed at improving the fit in the tail region between mathematical models and the actual clutter distribution, have been proposed. This report continues the study of the high grazing angle high resolution sea clutter, and particularly focuses on correlation and polarisation studies.

Both the correlation length in range and correlation time in azimuth are found to be shorter than those reported in the literature. This however may be attributed to the experimental conditions including high versus low grazing angles, high versus low resolutions and flying versus stationary or slow moving radar platforms. The analysis of the long-term correlations indicate that the wavelengths of wind waves and swells are retrievable from the range correlation whereas the periods of the wind waves and even swells are also recoverable from the azimuthal correlation.

The correlation between the HH and VV sea clutter data is low. A CA-CFAR (cell average constant false-alarm rate) processor applying a logical 'and' to the HH and VV sea clutter data would therefore increase the SCR (signal-to-clutter ratio). The improvement of the SCR is dependent on the shape parameter and is usually in a range of 3-to 5dB for the sea clutter analysed in the report. This is equivalent to the use of the incoherent integration of multi-pulse data to enhance clutter suppression and improve target detection.

Analysis of the polarimetric behaviour of sea clutter has suggested that at high grazing angles, an HH polarised radar outperforms a VV polarised radar in terms of target detection. For instance, in the region of $0 < cdf < 0.9999$, the HH sea clutter is constantly about 4 to 8dB lower than the VV sea clutter. The Cloude-Pottier Entropy-Alpha decomposition shows that the distribution of high grazing angle sea clutter spreads and covers a large portion of the feasible decomposition area indicating that scattering mechanisms of sea clutter are complex and multiple. It is also shown that the scattering mechanisms of the vertically polarised sea spikes that cause false alarms are simpler and often only one scattering mechanism is dominant in the VV spikes, whereas the HH spikes are more complex and often more than one scatterer contributes to the HH spikes.

The polarimetric analysis for target detection has also been discussed. To support the study, a C-band polarimetric SAR dataset collected by the NASA/JPL AirSAR system has been re-examined. Three groups of anchored small wooden vessels used as test targets were imaged in the dataset. A polarimetric decomposition technique has been applied to the dataset. The results indicate that while the sea surface is dominated by the Bragg scattering, the test vessels as well as urban areas are dominated by the double and odd bounce scattering mechanisms. Quantitative analysis indicates that the best polarisations, in terms of detecting targets on the sea surface, include double bounce, cross-slant 45^{o}, RR and HH polarisations. The other polarisations such as odd bounce, VV, HV, RL, co-45^{o} polarisations are not as good as the former set.

Author

Yunhan Dong
Electronic Warfare and Radar Division

Dr Yunhan Dong received his Bachelor and Master degrees in 1980s in China and PhD in 1995 at UNSW, Australia, all in electrical engineering. He then worked at UNSW from 1995 to 2000, and Optus Telecommunications Inc from 2000 to 2002. He joined DSTO as a Senior Research Scientist in 2002. His research interests are primarily in radar signal and image processing and clutter analysis. Dr Dong was a recipient of both the Postdoctoral Research Fellowships and Research Fellowships from the Australian Research Council.

Contents

1. INTRODUCTION 1

2. CORRELATION ANALYSIS 2
- **2.1 Dataset Descriptions 2**
- **2.2 Correlation Properties in Range and Azimuth 2**
  - 2.2.1 Short-Term Correlations 2
  - 2.2.2 Long-Term Correlations 7
- **2.3 Statistical Independence and Trend Tests 17**
  - 2.3.1 Run Test 17
  - 2.3.2 Reverse Arrangements Test 21
- **2.4 Correlation between HH and VV Data 26**

3. POLARIMETRIC BEHAVIOUR OF SEA CLUTTER 29
- **3.1 Target Detection: HH versus VV 29**
- **3.2 Entropy-Alpha Decomposition 32**

4. POLARISATION ANALYSIS FOR TARGET DETECTION 36
- **4.1 Polarisation Signatures of Common Scattering Mechanisms 36**
- **4.2 Re-examination of AirSAR data 39**
- **4.3 Four-Component Decomposition 47**

5. CONCLUSIONS 55

6. ACKNOWLEDGEMENT 56

7. REFERENCES 56

1. Introduction

The first phase of the Australian Defence Organisation’s (ADO) Project AIR 7000 envisages an acquisition of Multi-mission Unmanned Aerial Vehicles (MUAV) to enhance the capability of maritime surveillance. Airborne radar systems used for surveillance of ocean surface or low altitude atmosphere are affected by sea clutter which often seriously deteriorates or obscures radar echoes from targets of interests including ships, small vessels and air vehicles. The design of signal processors discriminating small targets from sea clutter requires a good understanding of characteristics of sea clutter.

The nature and characteristics of sea clutter depends on both sea conditions and radar parameters. Extensive studies of sea clutter have been reported in the literature in the last few decades (Long, 2001, Billingsley, 2002, Ward et al, 2006). Most of these studies, however, are based on sea clutter collected at low grazing angles. The grazing angle in these studies ranges from zero to several degrees, a typical configuration for applications of radars on ship or at coast. Maritime patrol aircraft views the sea surface at much higher grazing angles than ship or observatory. Since the dominant scattering mechanisms in sea clutter at low and high grazing angles are different, it would not be surprising if the nature and characteristics of the corresponding sea clutter are also different.

DSTO conducted a Sea Clutter Trial in 2004 (SCT04) in the Southern Ocean at a location approximately 100 km south of Port Lincoln in South Australia. Extensive sea clutter was collected in the trial using the DSTO developed X-band polarimetric airborne radar system (known as Ingara system). Details of the trial and sea clutter analysis have been reported elsewhere (Crisp et al, 2006).

A previous report has studied the statistical distribution of high grazing angle sea clutter from SCT04 (Dong, 2006). Models better than the traditional K- or Weibull distributions, aimed at improving the fit in the tail region between mathematical models and the actual clutter distribution, have been proposed.

This report continues the study of the high grazing angle sea clutter. Section 2 in particular carries out the correlation studies. It reveals that the wavelengths of wind waves and swells may be measurable from sea clutter correlation in the range direction (fast-time domain), and the period of the sea waves may also be measurable from sea clutter correlation in the azimuthal direction (slow-time domain). The polarimetric behaviour of the sea clutter is investigated in Section 3. To study the scenario of small targets (typical wooden vessels) embedded in sea clutter, a previously acquired C-band polarimetric SAR dataset collected by the NASA/JPL AirSAR system was re-examined, and various polarisations are studied to find the best polarisations which maximally discriminate targets from clutter.

2. Correlation Analysis

2.1 Dataset Descriptions

Using the Ingara radar system, SCT04 collected sea clutter data at incidence angles approximately varying from 45^{o} to 80^{o} on 8 separate days over a period of 18 days. Details of the trial may be found elsewhere (Crisp et al, 2006). This report primarily studies the datasets of run34690, collected on 16/08/04 at approximate 10:52 to 11:27 am local time. The radar was operated in the spotlight mode and the data processed as real aperture data. The radar flew along a circular orbit and looked approximately at the same spot with the same incidence angle but different azimuth angles. The run34690 consists of 71 separate datasets. Each contains 1024 range samples and approximate 950 azimuth samples which cover a span of approximately 5 degrees in azimuth. Table 1 lists the main parameters of the Ingara radar system used in this data collection.

Table 1: Radar parameters for run34690.

Parameter	Value
Centre frequency	10.1 GHz
Bandwidth of LFM	200 MHz
Polarisation	HH, VV, HV and VH
Pulse width	20 μs
Incidence angle	67.2^{o}
Azimuth angle	$0\text{-}360^{o}$
Altitude	1353 m
Nominal PRF*	540 Hz
Platform velocity	About 291 km/h
Range resolution	0.75 m
Azimuth 3dB beamwidth	2.4^{o}
Samples in range per pulse	1024

*Since the radar transmits the H and V polarised pulses interchangeably, the actual PRF for the HH or VV polarisation should be halved.

The wind speed at the approximate clutter collection time was about 7-9 m/s, retrieved from the Australian Government Bureau of Meteorology Automatic Weather Station data. The significant wave height was about 2.5 m recorded from a wave buoy deployed nearby. These parameters indicate the sea state to be about 2 on the Beaufort scale. The wind direction was also available (Crisp et al, 2006).

2.2 Correlation Properties in Range and Azimuth

2.2.1 Short-Term Correlations

Assuming a sample series $\{x(i), i = 1, 2, \cdots, N\}$ is wide sence stationary, the Pearson correlation coefficient $\rho(k)$ between $x(i)$ and $x(i+k)$ is defined as (Proakis and Manolakis, 1996, Stehwien, 1994, Sekine and Mao, 1990, Lombardo and Oliver, 1995),

$$\rho(k)=\frac{\left\langle x(i)x^{*}(i+k)\right\rangle-\left|\langle x\rangle\right|^{2}}{\left\langle |x|^{2}\right\rangle-\left|\langle x\rangle\right|^{2}} \qquad k=0,1,\cdots \tag{1}$$

where $\langle\cdot\rangle$ and $*$ denote the ensemble average and complex conjugate, respectively. The ensemble average is estimated by the usual way, for instance,

$$\langle x\rangle=\frac{1}{N}\sum_{i=1}^{N}x(i) \tag{2}$$

In the context of radar clutter, the series $\{x(i), i=1,2,\cdots,N\}$ denote amplitude or intensity of clutter echoes. The lag number k can be in either range or azimuth directions and will be clarified in the text accordingly. For instance, if the lag number k is in the range direction, $x(i)$ and $x(i+k)$ refer to as data collected in the ith and $(i+k)$th range bins from the same pulse (spatial measure). On the other hand, if the lag number k is in the azimuthal direction, $x(i)$ and $x(i+k)$ refer to as data collected in the same range bin but from the ith and $(i+k)$th pulses (temporal measure).

The correlation in the range direction (fast-time domain) can be considered as the spatial correlation because the data in different range bins are collected at the same azimuth angle, nearly the same incidence angle and time. The correlation in the azimuthal direction (slow-time domain) is a combination of temporal and spatial correlations since not only was the clutter collected from pulse-to-pulse but also the platform was flying. However the data used in this report was collected with the radar operated in the spotlight mode, so the correlation in azimuth can be considered primarily as the temporal correlation. Shown in Figure 1, Figure 2 and Figure 3 are the range (spatial) and azimuthal (temporal) correlation properties, calculated from run34690_255 (upwind), run34690_075 (downwind), and run34690_165 (crosswind), respectively. Correlation curves calculated from the simulated uncorrelated K-distributed data having the same shape and scale parameters as that of the sea clutter data are also shown for comparison. The correlation length is usually defined as the interval in which the correlation coefficient decays from 1 to $1/e=0.368$. If $\rho(k)<1/e=0.368$, the correlation is considered to be little or not correlated. From this sense, all correlations shown in Figure 1, Figure 2 and Figure 3 are low. Both range (spatial) and azimuthal (temporal) correlations achieve $\rho(k)<0.368$ for all $k\geq 1$.

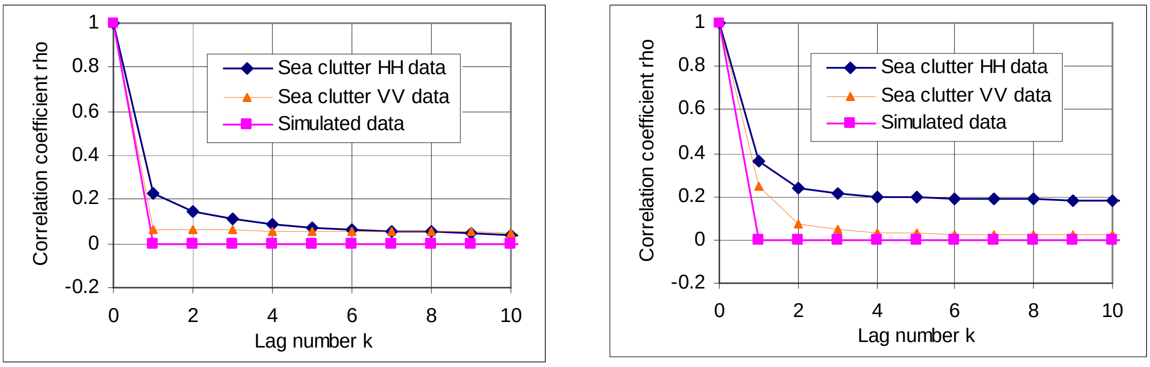

(a) range (spatial) correlation

(b) azimuthal (temporal) correlation

Figure 1: (a) range (spatial) and (b) azimuthal (temporal) correlations calculated from the dataset of run34690_225 (upwind).

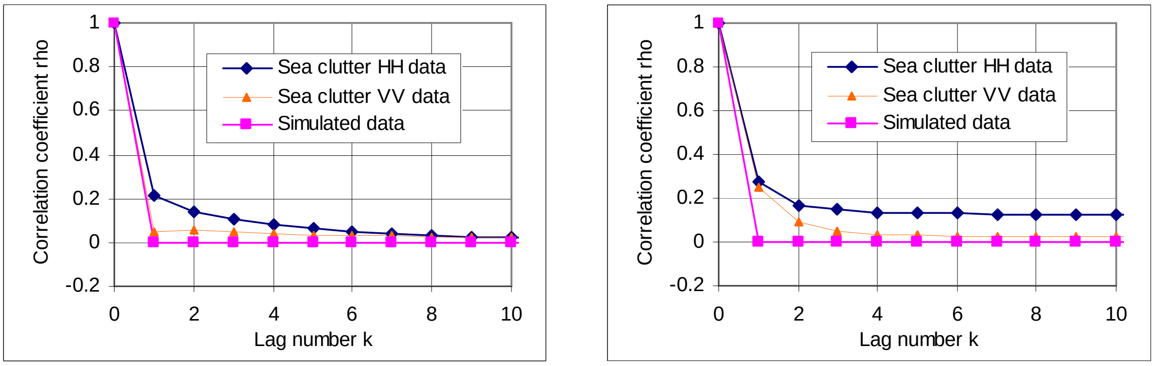

(a) range (spatial) correlation

(b) azimuthal (temporal) correlation

Figure 2: (a) range (spatial) and (b) azimuthal (temporal) correlations calculated from the dataset of run34690_075 (downwind).

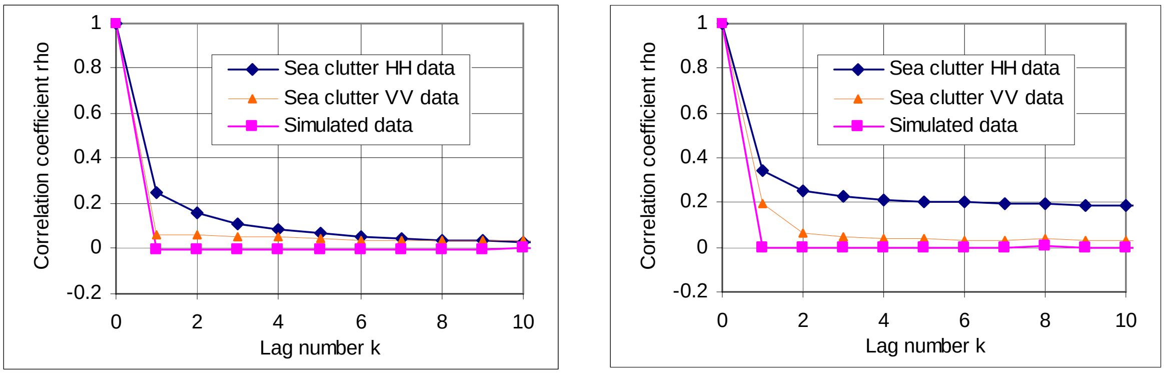

(a) range (spatial) correlation

(b) azimuthal (temporal) correlation

Figure 3: (a) range (spatial) and (b) azimuthal (temporal) correlations calculated from the dataset of run34690_165 (crosswind).

Although correlations in either range or azimuth are low, they are however higher than and different from the correlation of the simulated uncorrelated K-distributed data. The decay of the azimuthal correlations is slow and persistent, suggesting that there must exist a slow varying pattern in clutter azimuthal profiles that should be more observable, although there in fact also exit some pattern(s) in the range profile which however might be more subtle and less visually observable. To confirm this, we show in Figure 4 and Figure 5 clutter profiles of the HH and VV data, respectively. The profiles of the simulated uncorrelated K-distributed data are also shown for comparison. It can be seen that the azimuthal profiles of sea clutter, in particular the HH polarised data, exhibit an undulating pattern slower than that of the range profiles. As expected, there are no recognisable patterns in the simulated uncorrelated data.

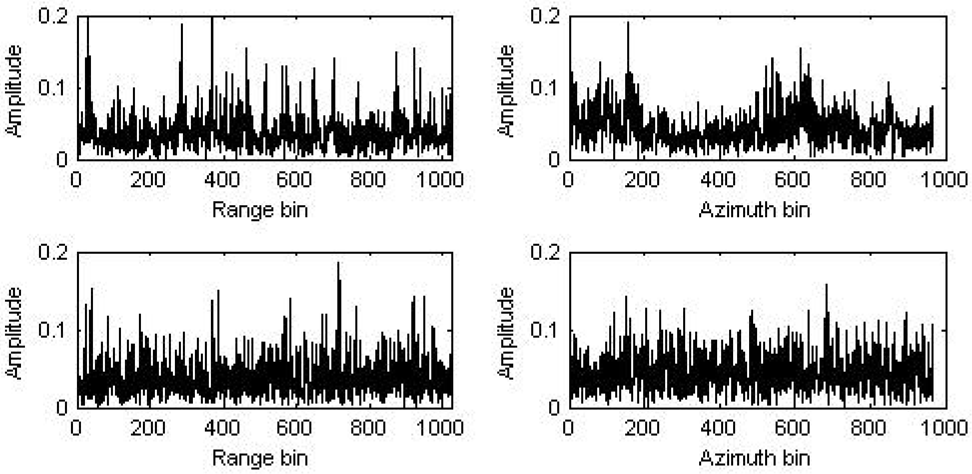

Figure 4: (top) Measured HH amplitude profiles in range and azimuthal directions, and (bottom) simulated amplitude profiles of the uncorrelated K-distributed data.

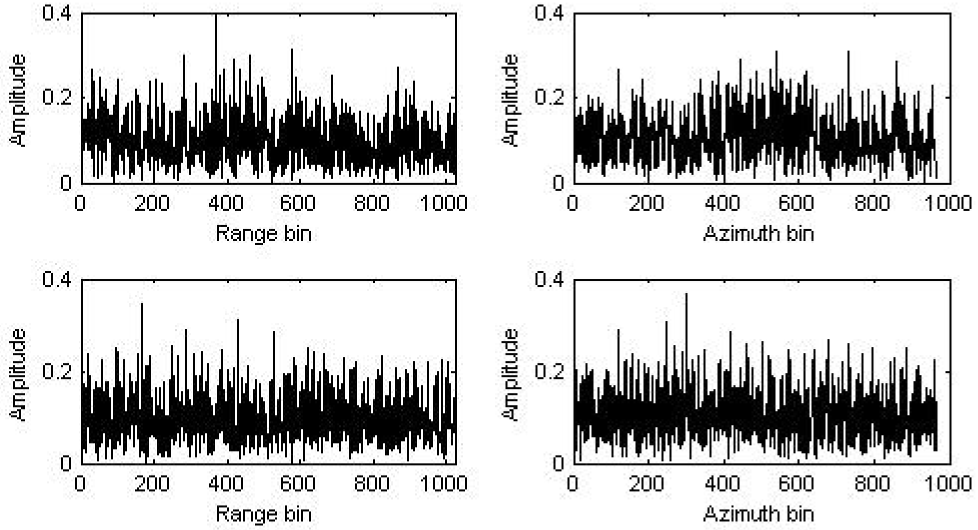

Figure 5: (top) Measured VV amplitude profiles in range and azimuthal directions, respectively, and (bottom) simulated amplitude profiles of the uncorrelated K-distributed data.

The correlation length in the range direction and the correlation time in the azimuthal direction measured by the Ingara X-band radar at the high grazing angle are found to be somewhat different from those measures at low grazing angle of about zero degrees, and published in the literature (Stehwien, 1994, Chan, 1990, Farina, et al, 1997). For instance, Stehwien (1994) has shown that $\rho(1) \approx 0.7$ and $\rho(2) \approx 0.4$ in the range direction for the X-band sea clutter data with conditions of sea state 2 (similar to the conditions of the datasets studied above), a grazing angle about 2° and range resolution of 2.14 m. The range correlation length would be about 4.5 m in this case.

The empirical correlation length ρ_L of the sea surface in the range direction for a fully developed sea is given by (Watts, 1996a),

$$\rho_L = \frac{\pi}{2}\frac{W^2}{g}(3\cos^2\delta + 1)^{1/2} \tag{3}$$

where W is the wind speed[1], g the acceleration of gravity and δ the angle between the line of sight of the radar and the wind direction. The wind velocity was about 7-9 m/s for the time when the datasets of run34690 were collected. The correlation length ρ_L according to (3) at $\cos\delta = \pm 1$ would be 15.7 to 26.0 m. The projection to the radar's range direction would be $\rho_L \sin\theta$, where θ is the incidence angle. The correlation measured by Stehwien (1994) is obviously much shorter than the value calculated by the empirical formula (3). The correlation length measured by the Ingara system is less than 1m, far from the prediction of (3). One obvious reason is that the sea observed was probably not fully

---

[1] The measurement of wind speed for this formula was taken at 10 metres above mean sea level (Watts, 1996a).

developed. Another reason might be that the formula was developed for low grazing angle situations, and thus does not suit high grazing angle situations.

It is well-known that the dominant scattering mechanisms of sea clutter at low grazing angles differ from those at high grazing angles (Long, 2001). Returns from multipath, shadowing and ducting mechanisms often dominate in sea clutter at low grazing angles, whereas the Bragg scattering from rough surfaces and scattering from whitecaps are the main contributions to sea clutter at high grazing angles. It is perhaps these differences in dominant scattering mechanisms that result in different correlation properties of sea clutter at low and high grazing angles.

The typical correlation time (azimuthal correlation) reported for X-band sea clutter at low grazing angles is about 10 ms (Chan, 1990). The measurement of Stehwien (1994) shows the correlation length in azimuth is about 10 pulses. Since he used a PRF of 1250 Hz, the correlation time is about 8 ms. Ward et al (2006, p. 20) indicate that the typical correlation time is about 5 to 10 ms. The correlation length in azimuth for the Ingara sea clutter is only about one pulse, i.e., about 4 ms. This may be attributed once again to the different conditions of measurement including (a) stationary versus movement of platform; (b) low versus high grazing angles, (c) high versus low PRFs and (d) low versus high radar resolutions. It is believed that a higher resolution results in a shorter correlation length in range and a shorter correlation time in azimuth.

2.2.2 Long-Term Correlations

The wavelengths and periods of sea surface seem to be retrievable from the analysis of power spectrum of long-time observations (Posner, 2002). From the definition of the correlation (1), it is easy to verify that the correlation of a sine function is still a sine function with the same frequency. As structures of sea waves and swells appear sinusoidal, if observed by a radar, it may be possible to retrieve the structural parameters of sea waves and swells from long-term correlations of sea clutter. One advantage of using correlation coefficients instead of original data to retrieve periodic parameters is that the correlation of randomly uncorrelated components is zero. Therefore, the correlation operation functions as a filter, which filters the uncorrelated components, and thus enhances the periodic components. Figure 6, Figure 7 and Figure 8 show the long-terms correlations measured from upwind, downwind and crosswind directions, respectively. It is seen that:

- For range correlations, frequencies of the slow periodic component of the HH and VV data shown in each figure are about the same. However, for the HH data, there also exist more obviously fast frequency components superposed on to the slow one.
- For the azimuthal correlations, it seems that only a very slow periodic pattern exists in both the HH and VV data.

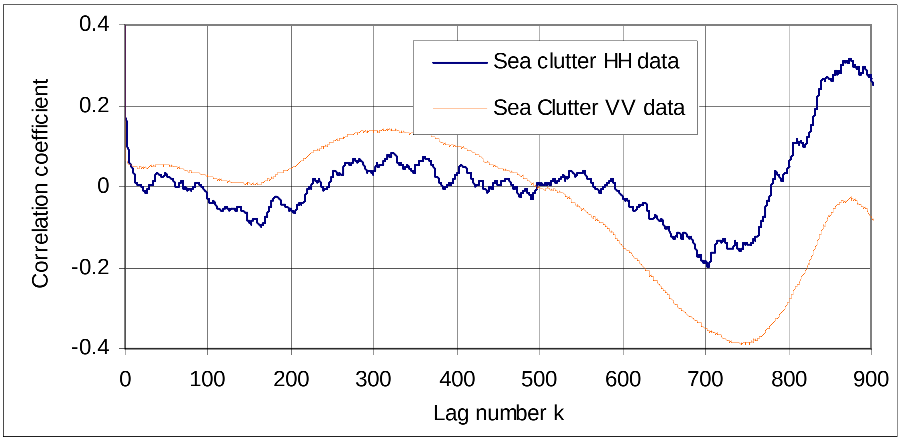

(a) range (spatial) correlations

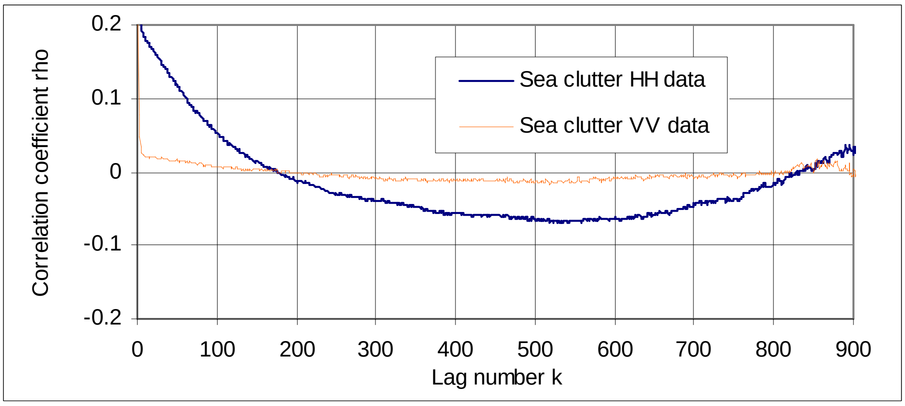

(b) azimuthal (temporal) correlations

Figure 6: Long-term (a) range (spatial) and (b) azimuthal (temporal) correlations calculated from the dataset of run34690_225 (upwind).

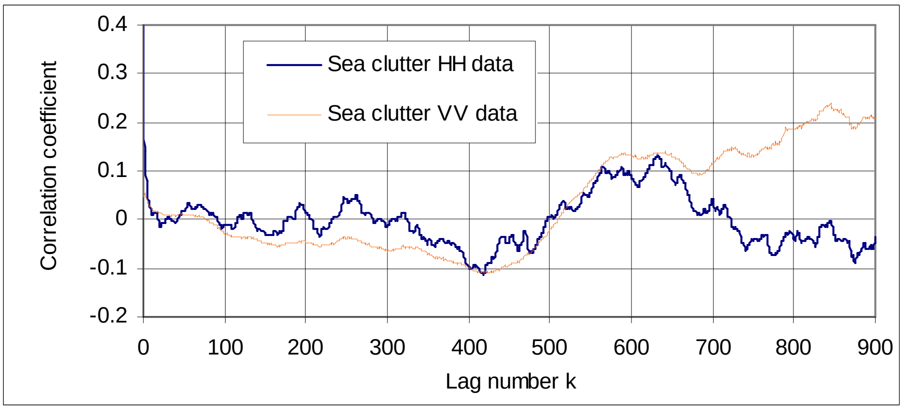

(a) range (spatial) correlations

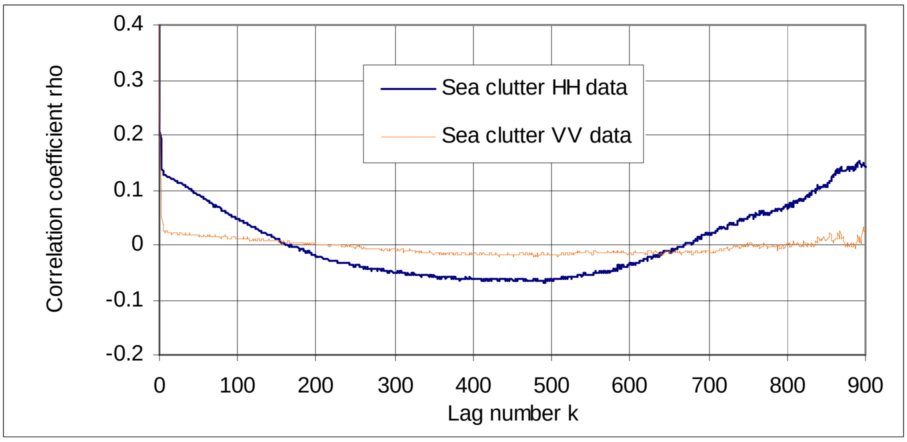

(b) azimuthal (temporal) correlations

Figure 7: Long-term (a) range (spatial) and (b) azimuthal (temporal) correlations calculated from the dataset of run34690_075 (downwind).

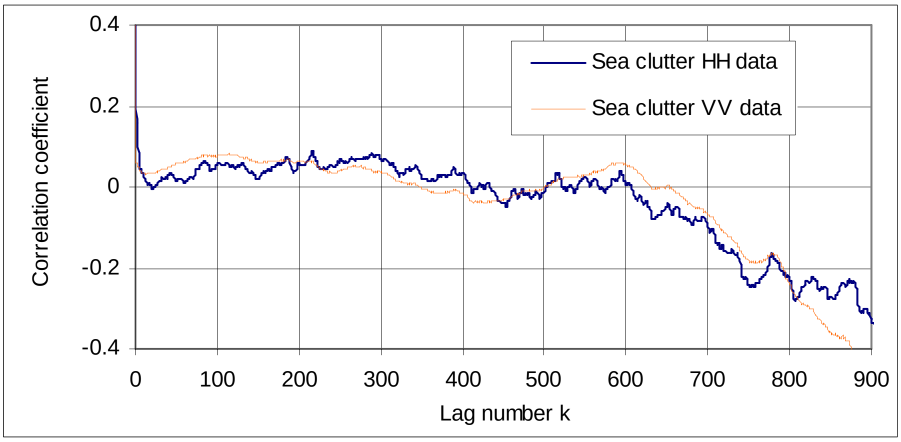

(a) range (spatial) correlations

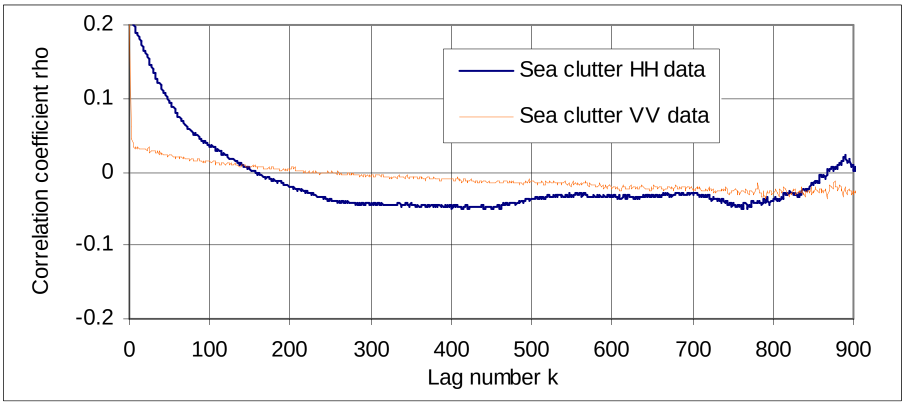

(b) azimuthal (temporal) correlations

Figure 8: Long-term (a) range (spatial) and (b) azimuthal (temporal) correlations calculated from the dataset of run34690_165 (crosswind).

To examine the dominant frequencies (wavelengths) in a correlation, the Chirp Fourier Transform (Porat, 1997, Chapter 5) was used to calculate the power spectra of correlation profiles. The frequency interval of the traditional Discrete Fourier Transform is $1/_{NT}$ Hz, where N and T are the number of samples and the sampling period, respectively. The frequency interval of the Chirp Fourier transform, on the other hand, can be arbitrarily chosen, so that peak frequencies of a spectrum can be estimated at a higher accurate level[2]. Figure 9, Figure 10 and Figure 11 show power spectra of range correlations of the HH and VV data for upwind, downwind and crosswind, respectively. The power spectra of azimuthal correlations of the HH and VV data for upwind, downwind, and crosswind,

---

[2] The use of zero padding and then Discrete Fourier Transform can also achieve a similar result. However caution should be exercised when using such transforms, the bottom line is that the discrete time-frequency transform is bounded by the uncertainty principle, and the infinite frequency intervals require infinite number of time measurements (Cohen, 1995).

respectively, are shown in Figure 12, Figure 13 and Figure 14. For simplicity, the labelled frequency assumes $\frac{1}{NT} = 1$. To reduce the bias, the first point $\rho(0) = 1$ was excluded in the spectrum calculation. A total of 900 points from $\rho(1)$ to $\rho(900)$ were used in the power spectrum calculation, but only the low frequency parts of the spectra are shown in the figures.

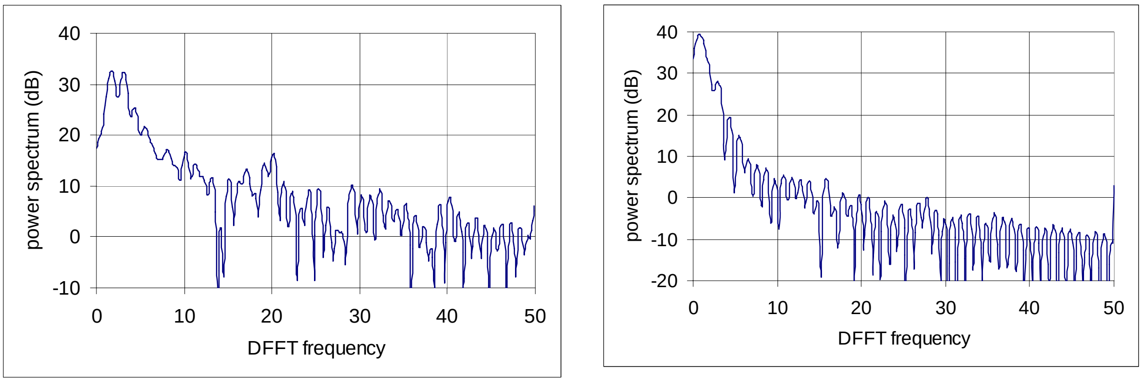

(a) HH *(b) VV*

Figure 9: Power spectra of the (a) HH and (b) VV range correlations (upwind).

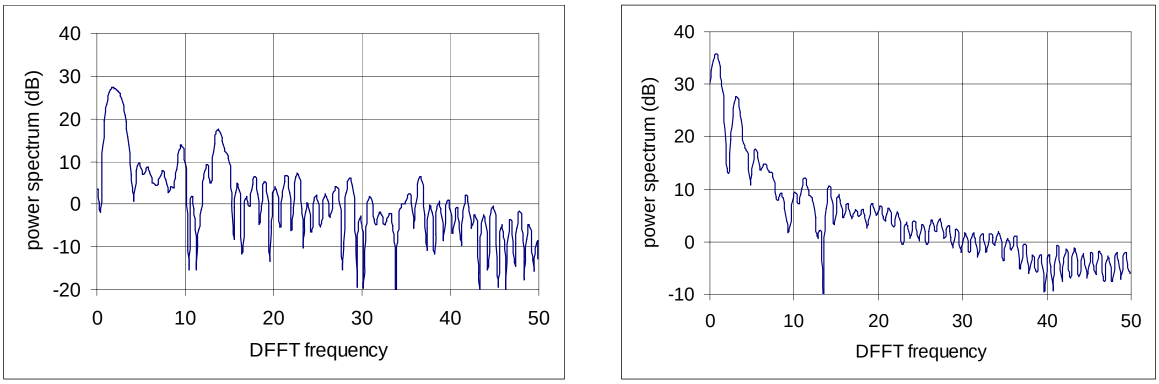

(a) HH *(b) VV*

Figure 10: Power spectra of the (a) HH and (b) VV range correlations (downwind).

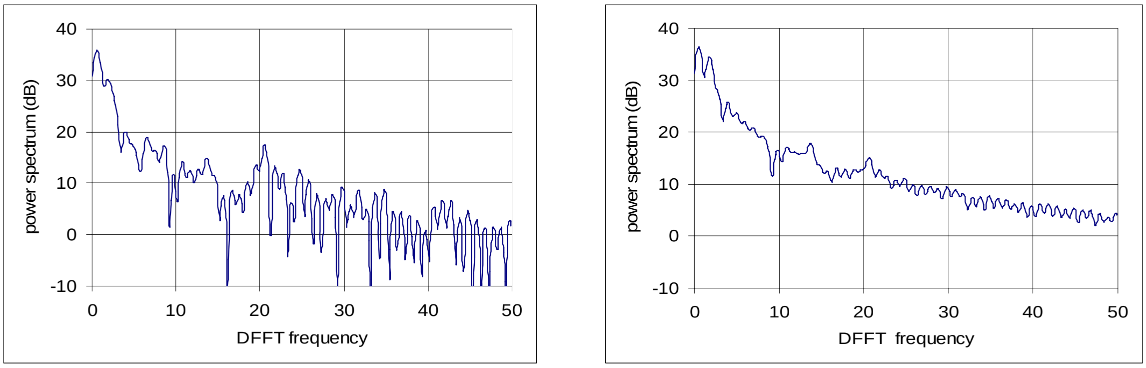

(a) HH

(b) VV

Figure 11: Power spectra of the (a) HH and (b) VV range correlations (crosswind).

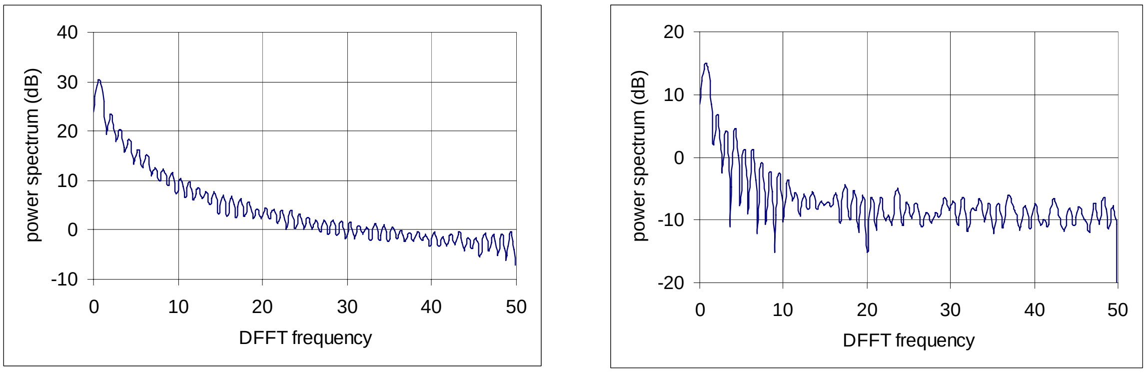

(a) HH

(b) VV

Figure 12: Power spectra of the (a) HH and (b) VV azimuthal correlations (upwind).

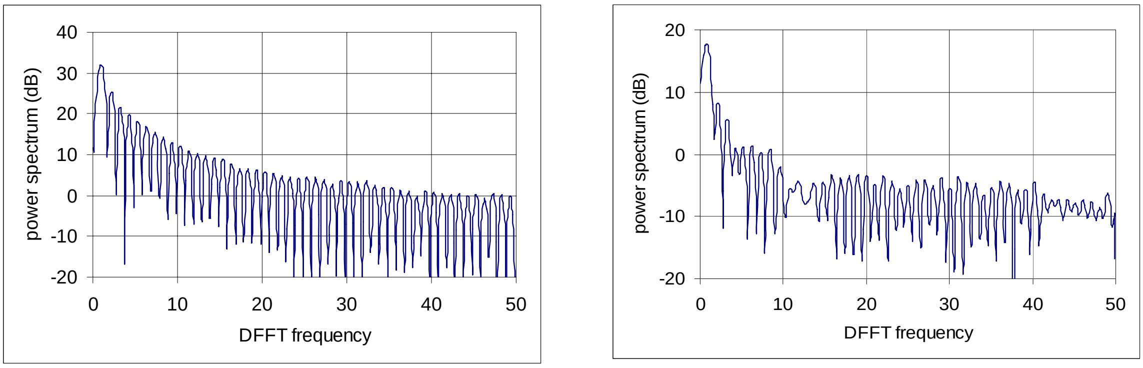

(a) HH

(b) VV

Figure 13: Power spectra of the (a) HH and (b) VV azimuthal correlations (downwind).

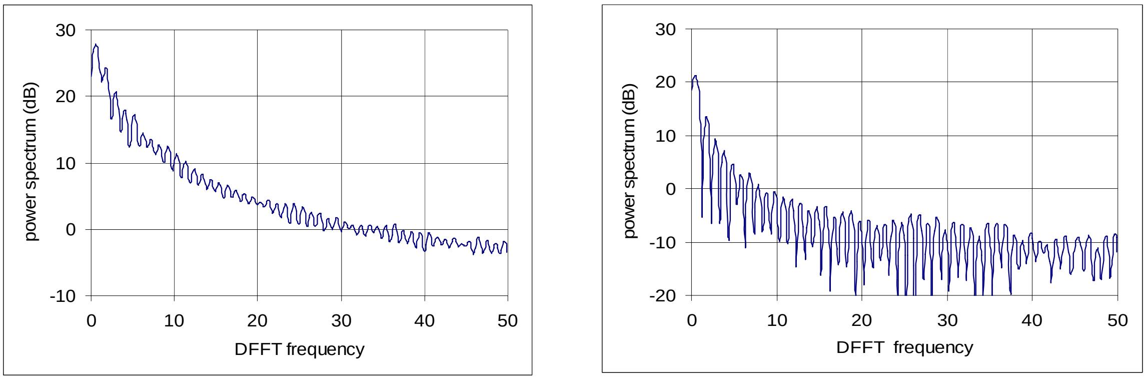

(a) HH *(b) VV*

Figure 14: Power spectra of the (a) HH and (b) VV azimuthal correlations (crosswind).

The spectra of the HV range and azimuthal correlations (upwind) are shown in Figure 15. In comparison with the spectra of the co-polarised correlations, it seems that the spectra of the cross-polarised correlations can only be able to retrieve the low frequency components which have higher energy. The high frequency components which have lower energy do not seem retrievable.

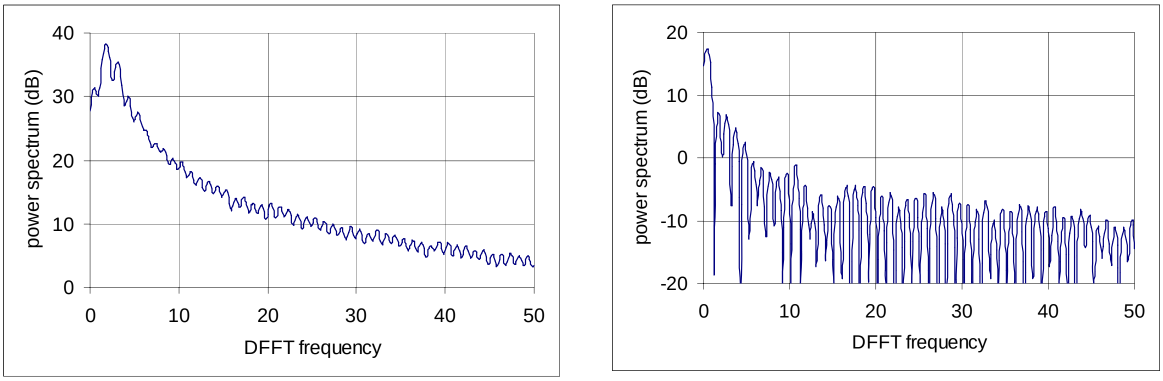

(a) HV, range *(b) HV, azimuth*

Figure 15: Power spectra of the (a) HV range and (b) HV azimuthal correlations (upwind).

The wavelength Λ of the dominant frequency f in the power spectrum of the range correlation can be computed once the dominant frequency is known. The formula is,

$$\Lambda = \frac{NT_{Range}\sin\theta}{f} \text{ (m)} \tag{4}$$

where $N = 900$ is the total number of the correlation points used in the transform, $T_{Range} = 0.75m$ is the radar resolution in range and θ is the incidence angle. The dominant frequencies in the spectra of range correlations and the corresponding wavelengths are listed in Table 2. Similarly the period of the dominant frequency in the spectrum of the azimuthal correlation can be computed by,

$$T = \frac{NT_{Azimuth}}{f} \text{ (s)} \tag{5}$$

where $T_{Azimuth} = 1/f_{PRF}$ is the sample period in the azimuth and f is the dominant frequency in the power spectrum of the azimuthal correlation. The results are listed in Table 3.

If we assume that the radar looked at the same spot and the period derived from the azimuthal correlation simply reflects the period of the wind wave, then the corresponding wavelength of the sea wave can be computed by (Pond and Pickard, 1978, Chapter 12),

$$\Lambda = 1.56T^2 \text{ (m)} \tag{6}$$

The calculated wavelengths are also listed in Table 3.

Table 2: Dominant frequencies of the power spectra of range correlations and the corresponding wavelengths.

Dataset	Polarisation	Frequency of dominant component*	Wavelength (m)
Run34690_255 (upwind)	HH	1.7, 3.1, 11.3, 20.2	366, 201, 55, 31
	VV	0.7, 2.9, 15.8	889, 215, 39
Run34690_075 (downwind)	HH	1.8, 9.6, 13.7	346, 64, 45
	VV	0.7, 3.4, 11.2	889, 183, 56
Run34690_165 (crosswind)	HH	0.6, 1.9, 6.6, 13.7, 20.6	1037, 328, 94, 45, 30
	VV	0.5, 1.8, 13.7, 20.7	1244, 346, 45, 30

*Nominal frequency assuming $1/_{NT} = 1$ in the Chirp Fourier transform.

Table 3: Dominant frequencies of the power spectra of azimuthal correlations and the corresponding periods and wavelengths.

Dataset	Polarisation	Frequency of dominant component*	Period (s)	Corresponding Wavelength** (m)
Run34690_255 (upwind)	HH	0.77	4.3	29
	VV	0.87	3.8	23
Run34690_075 (downwind)	HH	1.06	3.1	15
	VV	0.86	3.9	24
Run34690_165 (crosswind)	HH	0.66	5.1	41
	VV	0.57	5.8	52

*Nominal frequency assuming $1/_{NT} = 1$ in the Chirp Fourier transform. It should be pointed out that if the normal DFT were used, the frequencies of the dominant components in the power spectra of all azimuthal correlations would be the same and have a nominal frequency of 1.

**Calculated by the use of (6).

The directional ocean wave spectrum, at the time when the sea clutter run34690 was taken, recorded by a wave buoy deployed nearby is shown in Figure 16. The 2D spectra against frequency and direction, respectively, are shown in Figure 17. It can be seen that there are two dominant periodic components, whose frequencies are in the range of 0.065-0.080Hz and 0.018-0.019Hz, respectively. It is believed the former is corresponding to swell(s) and the latter to wind wave(s). The frequencies, periods and the corresponding wavelengths measured by the wave buoy are listed in Table 4.

Table 4: Dominated directional waves recorded by the wave buoy.

Wave	Direction (°)	Frequency (Hz)	Period (s)	Wavelength* (m)
Swell	230	0.065-0.08	12.5-15.4	244-369
Wind wave	80	0.18-0.19	5.3-5.6	43-48

*Calculated accordingly by the use of (6).

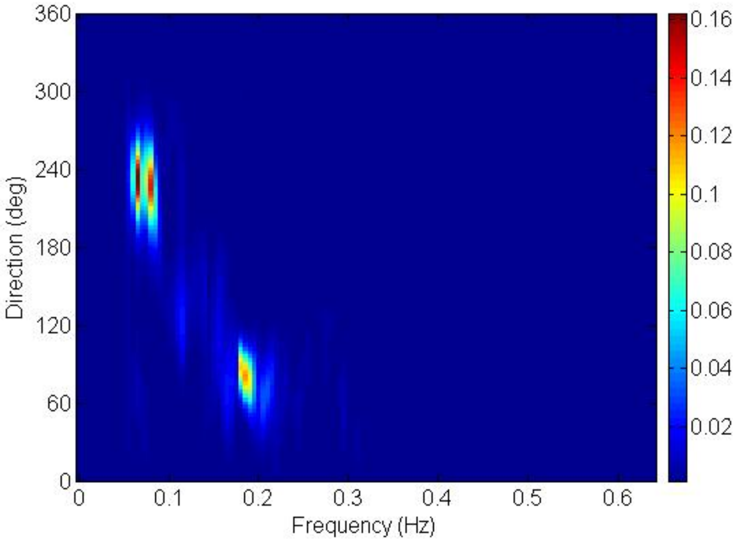

Figure 16: Ocean energy spectra (square metre per hertz per degree) recorded by the wave buoy on 16/8/06 at 11:20am local time (01:40UTC).

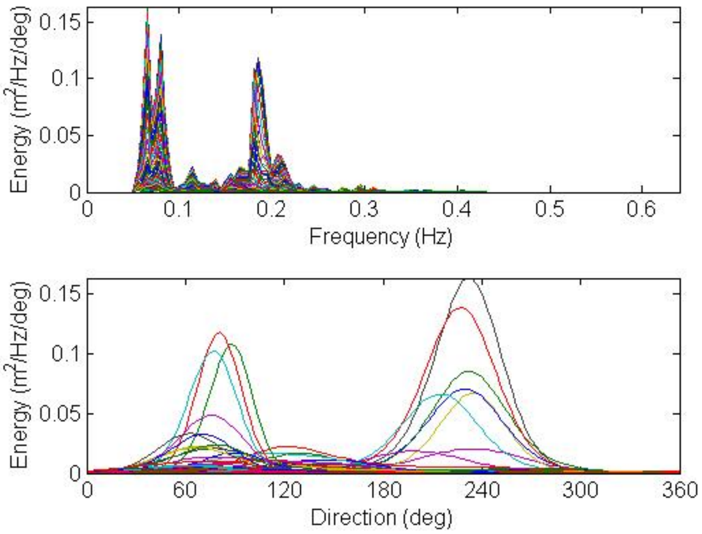

Figure 17: Ocean energy spectra against (top) frequency and (bottom) direction.

It can be seen that some wavelengths measured from the range correlations agree in general with the wavelengths derived from the wave periods recorded by the wave buoy. The discrepancies are existed and expected, as the radar measures more instantaneous sea surface features whereas the wave buoy's measurements are averaged from a much longer period. It is also noted that the range correlation of the HH data measures more frequency components than that of the VV data. The wavelengths measured by the HH and VV polarisations may also be different. Often the HH polarised antenna sees wind waves travelling faster than those seen by the VV polarised antenna. These phenomena have been attributed to nonlinear sea surface features, such as breaking waves and sharp wave crests (Posner, 2002, Trizna, 1991). Both Chan (1990) and Ward et al (1990) observed in the upwind direction that the dominant Doppler frequency of the HH data is higher than that of the VV data. The observations of Lee et al (1996) are more interesting. They found that with an increase in grazing angle, the difference of the dominant Doppler frequencies of the HH and VV data disappears. Table 2 shows that the lowest wavelength (which has the highest power spectra) of the HH data in upwind and downwind directions is somewhat shorter than that of the VV data, indicating that the dominant Doppler frequency of the HH data would still be higher. In another words, different polarisations view different parts of wave structures even at a high grazing angle. As shown in Figure 15, the HV range correlation can only be able to measure the very dominant wave having highest energy, which in this case is the swell.

The azimuthal correlation would not be able to measure the periods of longer wavelengths on this occasion because the observation geometry cannot be maintained due to movement of the platform. Since a longer observation period in the azimuth is required should the longer periods of wavelengths become retrievable form the azimuthal correlation profiles. This should not be an issue for a stationary or slow moving platform. For a fast moving platform, such as aircraft, this might impose a difficulty in practice, as the observation geometry would have been changed significantly along with the movement of the platform over a long period even if the radar is operated in the spotlight mode.

The above correlation analysis is very promising and suggests that sea surface characteristics, such as various wavelengths and periods of wind waves and swells, may be measurable by radar. The range correlation in general can directly measure wavelengths of wind waves and swells, whereas the azimuthal correlation in general can directly measure periods of wind waves and swells. It should be pointed out that a wavelength measured by the range profile and a period measured by the azimuthal profiles are the direct measurements, and they do not necessarily obey (6) which is only correct for a fully developed deep sea. It also be noted that since the periods of swells are long, a long observation is required if one wants to directly retrieve the periods of swells from the azimuthal correlation. Once the wavelengths and periods are known for a fully developed deep water sea, the sea states may also be estimable without a need of directly in-situ measurement of physical parameters including wind, wavelength, wave period and height etc., which are often difficult to obtain in practice.

Although the long-term correlation can reveal sea surface structural parameters, the values of the correlation coefficients are low. This fact indicates that the dominant scatterers (first-order) such as break waves and whitecaps are uncorrelated either temporally or spatially resulting in low correlation coefficients. The correlated part is due to non-dominant scatterers (second-order), possibly the periodic undulating surfaces, so that the parameters of the periodic undulating surfaces can become retrievable. In this sense, a sea surface may be modelled as a combination of non-dominant but correlated scatterers (periodic undulating surfaces) and dominant but random and uncorrelated scatterers (whitecaps, breaking waves and etc).

2.3 Statistical Independence and Trend Tests

The preceding subsection has studied correlation properties of the sea clutter collected in SCT04. Statistical independence and underlying trends of the sea clutter is further tested in this subsection. Given a sample series, its statistical independence and underlying trends can be tested using relevant hypothesis tests. Two such popular procedures are run test and reverse arrangements test (Bendat and Piersol, 1986).

2.3.1 Run Test

Run test is a nonparametric and distribution free test. It is powerful for detecting underlying fluctuating trends (Bendat and Piersol, 1986). Given a sample series $\{x(i), i = 1, 2, \cdots, N\}$, let all samples with a value greater (less) than the median value of the series be identified by 1 (0). The resulted observations only contain 1 or 0. For observations comprised of 1 and 0, such as $\{1\,1\,0\,1\,0\,0\,0\,1\,1\,0\,0\,1\}$, a run is defined as a sequence of identical observations that is followed and preceded by a different observation or no observation at all. For instance the above sequence of observations has 7 runs. The number of runs that occur in a sequence of observations gives an indication as to whether or not the results are independent random observations of the same random variable.

Specifically, if a sequence of N observations are independent observations of the same random variable, that is, the probability of 1 or 0 does not change from one observation to the next, then the sampling distribution of the number of runs in the sequence is a random variable r with a mean and variance as follows (Bendat and Piersol, 1986):

$$\mu_r = \frac{N}{2} + 1 \tag{7}$$

$$\sigma_r^2 = \frac{N(N-2)}{4(N-1)} \tag{8}$$

Let it be hypothesised that the observations are independent, the acceptance region of this hypothesis is

$$r_{N/2;1-\alpha/2} < r \leq r_{N/2;\alpha/2} \tag{9}$$

where α is the level of significance for acceptance. Since r is normally distributed, the upper and lower bounds of the acceptance region can be computed by,

$$r_{N/2;1-\alpha/2} = \mathrm{int}\{-\sigma_r z_{\alpha/2} + \mu_r - 1\} \tag{10}$$

$$r_{N/2;\alpha/2} = \mathrm{int}\{\sigma_r z_{\alpha/2} + \mu_r\} \tag{11}$$

where $\mathrm{int}\{\cdot\}$ is a function rounding a value to its nearest integer, $z_{\alpha/2}$ may be found from the integral $\frac{\alpha}{2} = \frac{1}{\sqrt{2\pi}} \int_{z_{\alpha/2}}^{\infty} \exp(-t^2/2)\, dt$. For instance, $z_{0.025} = 1.96$ corresponds to a one-sided significance of 0.025.

The number of runs for the upwind HH and VV amplitude samples in the range direction with the sample lengths of 40, 200, and 1000 per pulse are shown in Figure 18, Figure 19 and Figure 20, respectively. For comparison, shown in the figures is also the number of runs for the simulated uncorrelated (independence) K-distributed samples with the same shape and scale parameters as the HH or VV data. The upper and lower bounds shown in each figure correspond to the $\alpha = 0.05$ level of significance. It can be seen that the most of runs of the simulated data, regardless of their lengths, are confined within the boundary, which means that the hypothesis that the samples are independent without any underlying trends is acceptable at the $\alpha = 0.05$ level of significance. Those few exceptions whose runs are out of the boundary is an indication of a Type I error, that is for these few occasions the hypothesis is rejected at the given $\alpha = 0.05$ level of significance (due to the number of runs out of the boundary) when in fact it is true. The probability of a Type I error is equal to α, that is, the chance that the hypothesis is rejected while the hypothesis in fact is true is 5%.

The distribution of r for the sea clutter is however dependent on the length of samples and the polarisation. When $N = 40$, the distribution of r are very similar to that of the simulated uncorrelated data, indicating, the underlying trends of the data are not observed (due to in fact that the underlying change is slow), and hence the data can be considered as uncorrelated (independence). However with increasing in observation length, the number of runs decreases. For instance, the majority of r_{1000} for the HH data are out of the boundary, suggesting that the hypothesis that the data samples are independence and without underlying trends should be rejected.

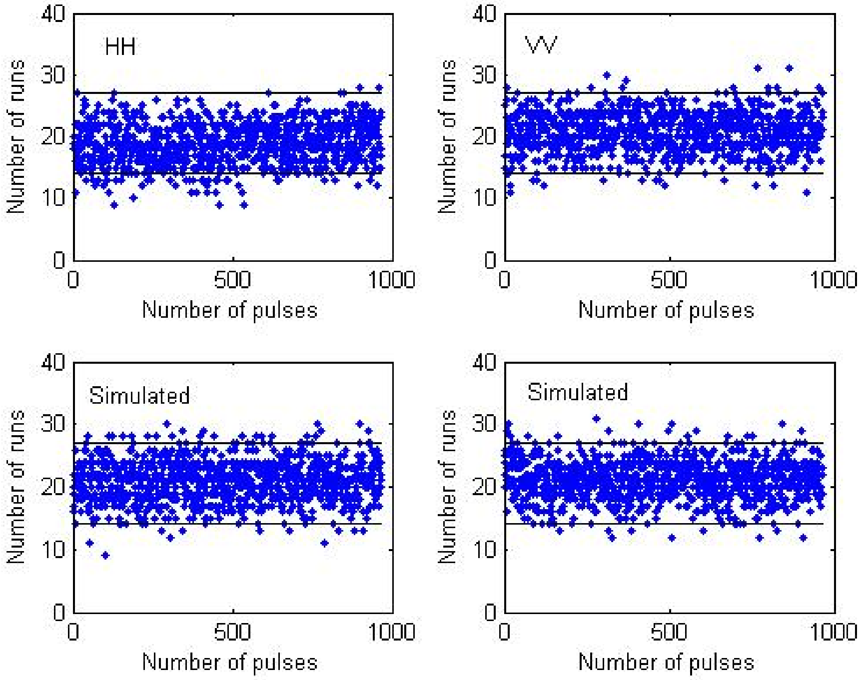

Figure 18: Run tests for 40 amplitude range samples per pulse. The number of runs for the simulated uncorrelated K-distributed samples that have the same shape and scale parameter as the HH or VV data are also shown for comparison.

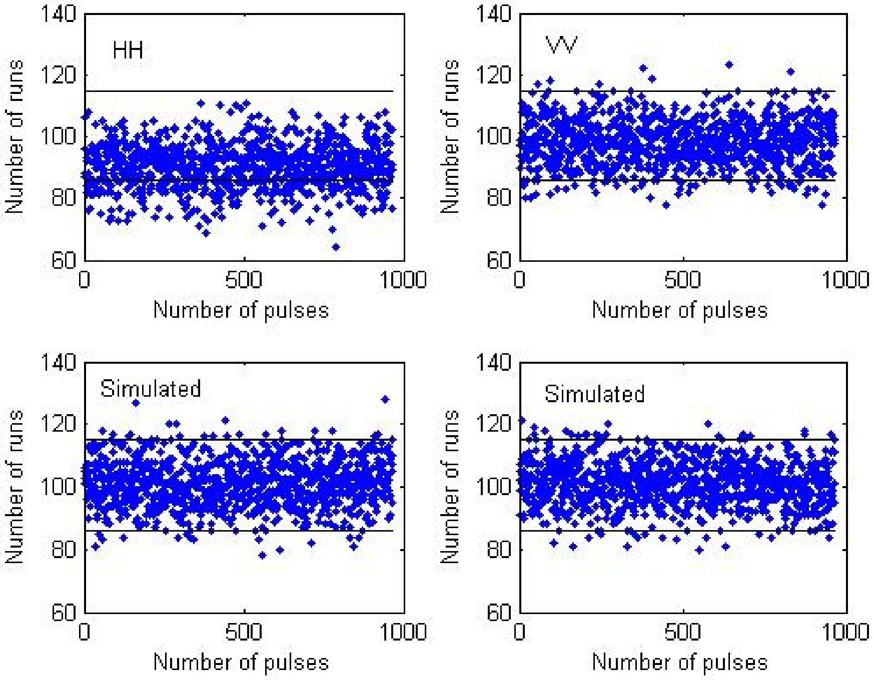

Figure 19: Run tests for 200 amplitude range samples per pulse. The number of runs for the simulated uncorrelated K-distributed samples that have the same shape and scale parameter as the HH or VV data are also shown for comparison.

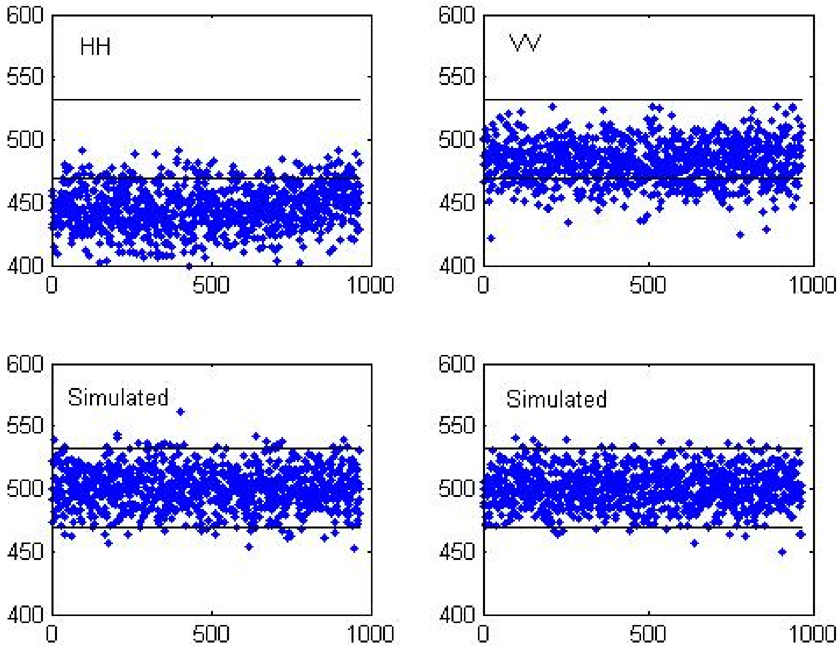

Figure 20: Run tests for 1000 amplitude range samples per pulse. The number of runs for the simulated uncorrelated K-distributed samples that have the same shape and scale parameter as the HH or VV data are also shown for comparison.

2.3.2 Reverse Arrangements Test

Reverse arrangements test is powerful for detecting underlying monotonic trends. For a sequence of N observations of a random variable x, count the number of times that $x_i > x_j$ for all $i < j \le N$, $i = 1, 2, \cdots, N-1$. Each such inequality is called a reverse arrangement. The total number of reverse arrangements is denoted by A. If the sequence of N observations are independent observations of the same random variable, then the number of reverse arrangements is a random variable A with a mean and variance as follows (Bendat and Piersol, 1986):

$$\mu_A = \frac{N(N-1)}{4} \tag{12}$$

$$\sigma_A^2 = \frac{N(2N+5)(N-1)}{72} \tag{13}$$

Let it be hypothesised that the observations are independent, the acceptance region of the hypothesis is

$$A_{N;1-\alpha/2} < A \le A_{N;\alpha/2} \tag{14}$$

where α is the level of significance for acceptance. Since A is normally distributed, the upper and lower bounds of the acceptance region can be computed by,

$$A_{N;1-\alpha/2} = \text{floor}\{-\sigma_A z_{\alpha/2} + \mu_A\} \tag{15}$$

$$A_{N;\alpha/2} = \text{floor}\{\sigma_A z_{\alpha/2} + \mu_A\} \tag{16}$$

where $\text{floor}\{\cdot\}$ is a function rounding a value to its nearest integer less than or equal to that value.

The number of reverse arrangements for the upwind HH and VV amplitude samples in the range direction with the sample lengths of 40, 200, and 1000 per pulse are shown in Figure 21, Figure 22 and Figure 23, respectively. For comparison, the number of reverse arrangements for the simulated uncorrelated (independence) K-distributed samples with the same shape and scale parameters as the HH or VV data is also shown. The upper and lower bounds shown in each figure correspond to the $\alpha = 0.05$ level of significance. It can be seen that the number of reverse arrangements for the most of simulated data, regardless of their lengths, is confined within the boundaries, which means that the hypothesis that the samples are independent without any underlying trends is acceptable at the $\alpha = 0.05$ level of significance. Those few exceptions whose reverse arrangements are out of the boundary is an indication of a Type I error, that is the hypothesis is rejected at the given $\alpha = 0.05$ level of significance (due to the number of reverse arrangements out of the boundary) when in fact it is true.

The distribution of A for the sea clutter however varies with the length of samples and the polarisation. The distribution of A for the HH clutter even starts showing a pattern for $N = 40$, different from the result of the run test, indicating that the reverse arrangements test is more sensitive for detecting monotonic trends. The underlying trends in the VV data seem to become more detectable only when N becomes larger. On the other hand, with a long observation of the HH clutter, the underlying monotonic changes becomes periodic changes, and therefore, the underlying trends become less detectable using the reverse arrangements test. In this case, the run test is more powerful.

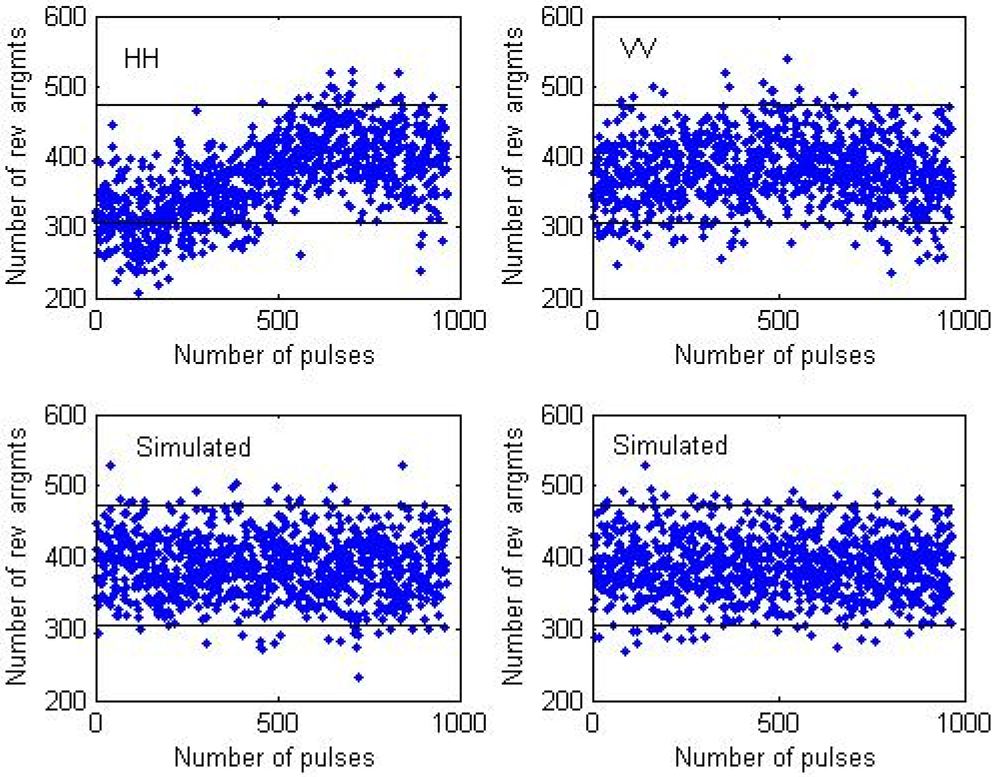

Figure 21: Reverse arrangements test for 40 amplitude range samples per pulse. The number of reverse arrangements for the simulated uncorrelated K-distributed samples that have the same shape and scale parameter as the HH or VV data are also shown for comparison.

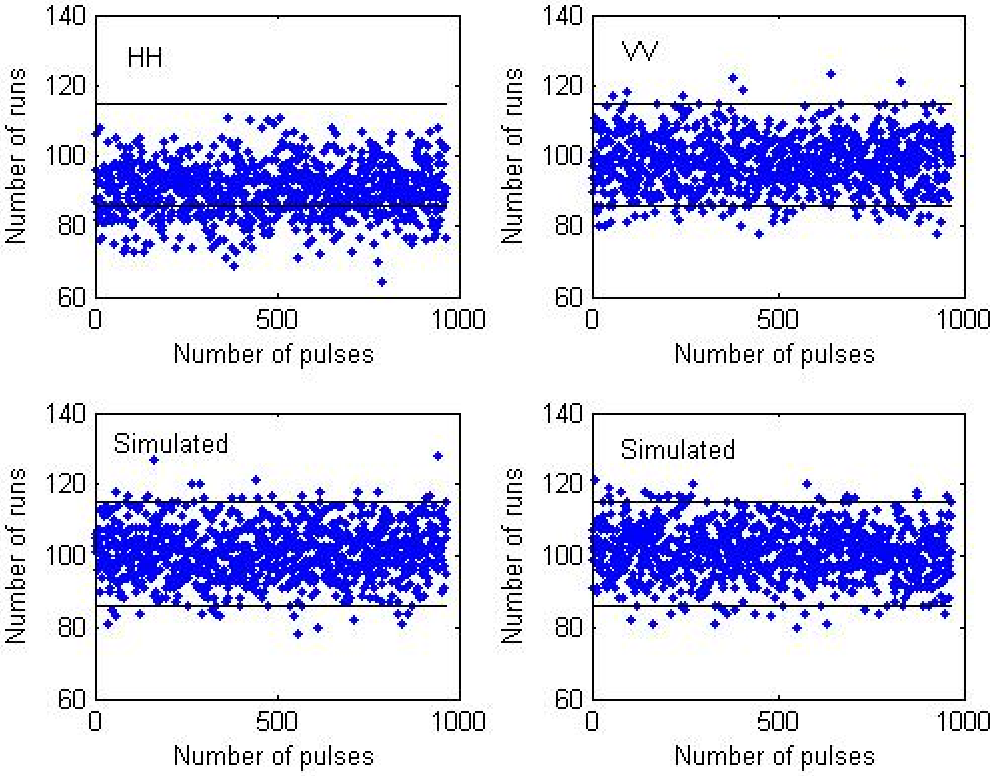

Figure 22: Reverse arrangements test for 200 amplitude range samples per pulse. The number of reverse arrangements for the simulated uncorrelated K-distributed samples that have the same shape and scale parameter as the HH or VV data are also shown for comparison.

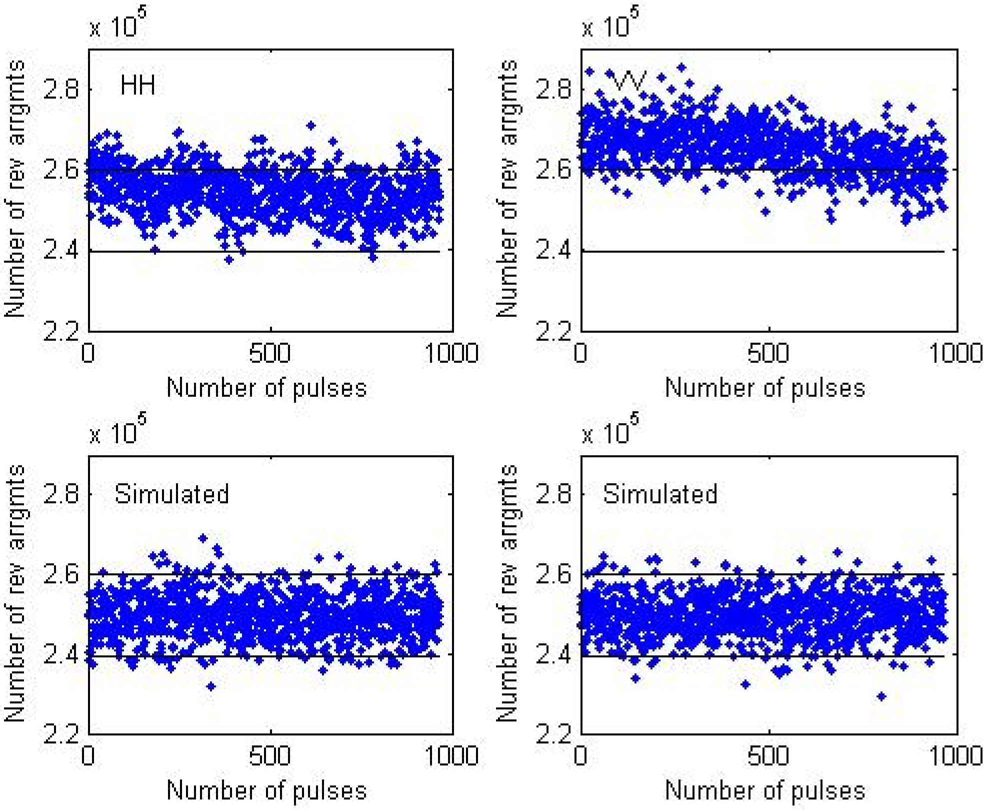

Figure 23: Reverse arrangements test for 1000 amplitude range samples per pulse. The number of reverse arrangements for the simulated uncorrelated K-distributed samples that have the same shape and scale parameter as the HH or VV data are also shown for comparison.

The above results of run test and reverse arrangements test are consistent with the preceding correlation analysis and the known sea clutter features. Sea clutter (in range direction) may be modelled by two main components, with one fast varying component modulated by a slow varying component (Watts, 1985, Ward et al, 1990). The fast varying component is also referred to as speckle while the slow varying component, sometimes called the texture, has connections with wave structures. For the clutter studied in this report, the fast varying component is proven to be largely uncorrelated by the short-term correlation, as well as run test and reverse arrangements test with short length observations. The slow varying component is detectable by the long-term correlation or run test and reverse arrangements test with a long observation length. It is also found that the HH sea clutter data often contains more high frequency components than the VV data. This claim is supported by more obvious harmonics in the HH correlation curves, and the easier detection of fluctuating trends by the run test and monotonic trends by the reverse arrangements test.

An understanding of above sea clutter features is important. For instance, a CA-CFAR processor often uses the average of measurements in a small sliding window to adaptively adjust the detection threshold. Because the length of the sliding window is usually short, the samples in the sliding window can be considered to be uncorrelated to simplify the algorithm. On the other hand if an algorithm involves a long processing window, the effect of the slow varying component has to be taken into account.

2.4 Correlation between HH and VV Data

Chan (1990) observed that horizontally and vertically polarised sea clutter show different Doppler properties, and normally the Doppler shift of a horizontally polarised sea clutter spectrum is greater than that of vertically polarised sea clutter under similar sea conditions. These observations indicate that the dominant scattering mechanisms of sea clutter with different polarisations are different. Therefore, we can expect that the correlation between the HH and VV sea clutter data would be low. A realisation of the probability density function (pdf) $p(x, y)$ of sea clutter amplitude for the dataset of run34690_255 containing approximately 10^6 data samples is shown in Figure 24, where x and y are amplitudes of the VV and HH sea clutter data, respectively. The marginal distribution, i.e., the integration of $p(x, y)$ with respect to x or y would give the pdf of the HH or VV data. It can be seen that the correlation between the HH and VV data are indeed very low, and the probability of high returns simultaneously measured by both the horizontally and vertically polarised antennas are significantly lower than that measured by either of the two antennas. Utilising this property, we may design a CFAR scheme, which declares presence of a target in a range bin only if both the HH and VV returns of the bin simultaneously exceed the respective H and V thresholds, to significantly reduce the false-alarm rate. To demonstrate, global fixed thresholds for the HH and VV clutter is depicted in Figure 24. The false-alarm rates for the HH or VV data would be the integrals of $\iint_{I+III} p(x, y)dxdy$ or $\iint_{II+III} p(x, y)dxdy$. However the false-alarm rate would reduce to $\iint_{III} p(x, y)dxdy$ if both the HH and VV returns simultaneously exceed their corresponding thresholds. On the other hand, it is believed that in general the correlation between the HH and VV measures of a target is high, so the target detection probability would remain approximately unchanged with such a CFAR scheme. In practice, we can decrease the H and V thresholds so that the false-alarm rate of area III is kept at the same level as if only the HH data or VV data is used. Decreasing the threshold is equivalent to increasing the target detection probability. In another word, we increase the signal-to-clutter ratio (SCR) by utilising the correlation property between the HH and VV data.

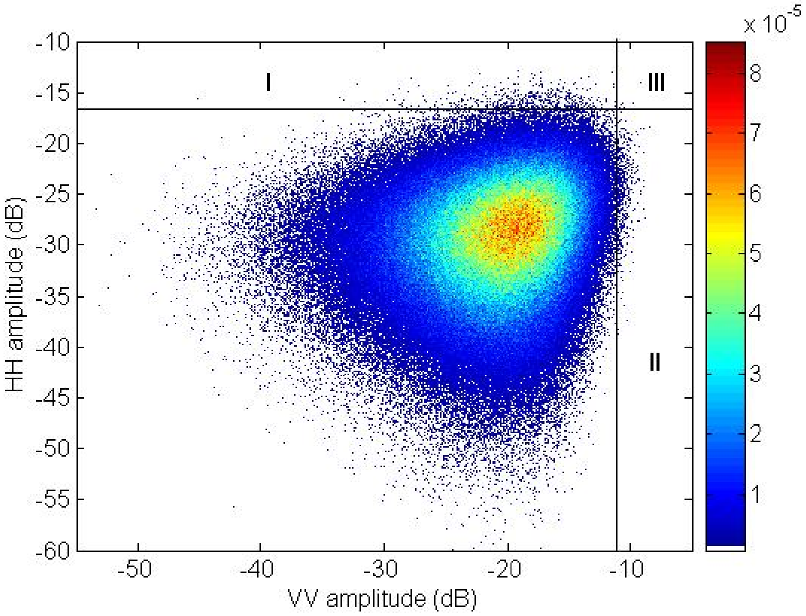

Figure 24: Sea clutter amplitude pdf with respect to the vertical and horizontal polarisations for the dataset of run34690_255. If a fixed global threshold for a CFAR scheme were used for the HH or VV data, the false-alarm rates would be the integrals of the pdf in areas I and III for the HH data, and II and III for the VV data, respectively. However if a CFAR scheme specified both the HH and VV data simultaneously exceeding their corresponding thresholds, the false-alarm rate would reduce to the integral of the pdf in area III only.

To examine the SCR improvement, we applied a CA-CFAR scheme to both the HH and VV data with a specified false-alarm rate. The samples that exceed the thresholds are further examined, and only those samples whose HH and VV values exceed the thresholds simultaneously are considered as the final false-alarm output. According to the previous studies, the K distribution is a better fit than the Weibull distribution for sea clutter, although both distributions poorly model empirically derived clutter distributions in the tail region (Dong, 2006). Since the CA-CFAR threshold for Weibull distributed data has been given in a closed form and such a closed form threshold for the K distributed data does not exist (the threshold can however be numerically determined if the shape parameter of the K distribution is known), we assume the sea clutter is Weibull distributed for simplicity. The CA-CFAR threshold T for Weibull distributed data is (Dong, 2006),

$$P_{fa} = \frac{1}{\left[1+\left(T/r\right)^{b}\right]^{N}} \qquad (17)$$

where

$$r = \frac{\Gamma(N+1/b)}{N\,\Gamma(N)\Gamma(1+1/b)} \qquad (18)$$

N is the size of the process window ($N = 24$ was used in this report), b is the shape parameter of the Weibull distribution and $\Gamma(\cdot)$ is the gamma function. In general the Weibull fit is conservative, i.e., its cumulative distribution function (cdf) converges a little faster than that of actual sea clutter data especially for the horizontally polarised data (Dong, 2006). In the calculation, for a nominal false-alarm rate $P_{fa} = 10^{-3}$, we used $1.2T$ as a actual threshold for the HH data to reduce the discrepancies between the nominal and actual false-alarm rates. No such modification was needed for the VV data. The process was applied to all 71 datasets of run34690. Each dataset contains about 10^{6} samples consisting of 1024 samples in range and about 960 samples in azimuth corresponding to an approximate 5° span in azimuth. The process first estimates the shape parameters for each HH and VV dataset separately. The appropriate thresholds are calculated accordingly. With a sliding window, all samples are passing though the CA-CFAR estimator, the actual false-alarm rates for the HH and VV data were obtained, which serves as an assessment of the threshold (17). Finally, samples whose HH and VV values exceed the H and V thresholds simultaneously (i.e., a logical 'and' operation is applied) were counted to provide the actual final false-alarm rate for utilising the correlation property between the HH and VV data. The results are shown in Figure 25. It can be seen that the threshold given in (17) can control the actual false-alarm rate at a reasonably good level as specified (in this case, $P_{fa} = 10^{-3}$). The final false-alarm rate of both the HH and VV simultaneously exceeding their corresponding thresholds is about one order lower. In another word, we utilise the correlation properties between the HH and VV data to significantly reduce the false-alarm rate. This can be viewed as an improvement of the SCR. The actual value of the improvement of the SCR can be evaluated by examining the difference between 1-cdf equal to the nominal false-alarm rate and the actually achievable false-alarm rate from the clutter distribution. This difference depends on the shape parameter and is usually in a range of 3 to 5 dB for the sea clutter analysed in this report.

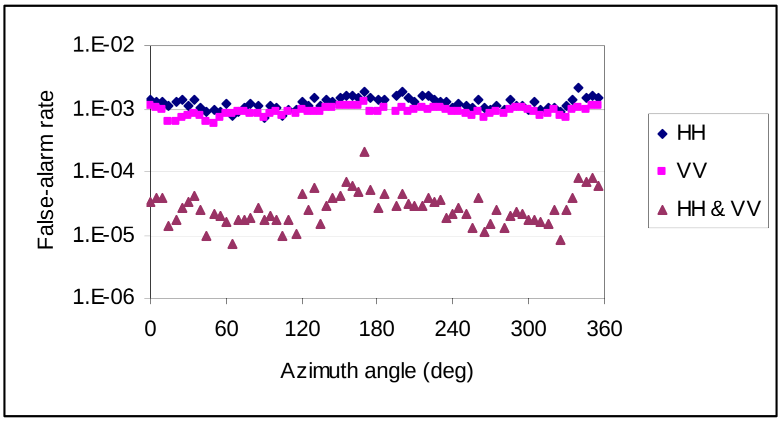

Figure 25: False-alarm reduction by utilising correlation properties of the HH and VV data. The top lines are the actual false-alarm rates for the HH and VV data, respectively, when the nominal false-alarm rates were set to 10^{-3}. *If we only count samples, whose HH and VV values exceed the H and V thresholds simultaneously, as false targets, the actual false-alarm rate is then generally reduced to below* 10^{-4}.

Despite no data to support the analysis, it is evident that scan-to-scan single polarisation sea clutter data should also exhibit little correlation as long as the time interval between the successive scans is greater than the correlation time, conservatively say, about 10ms. Therefore using the integration of scan-to-scan or pulse-to-pulse with frequency agility data should also suppress sea clutter and improve the SCR.

3. Polarimetric Behaviour of Sea Clutter

3.1 Target Detection: HH versus VV

The detection performance of a radar system in sea clutter is dependent on a range of factors. The performance of non-coherent radars primarily depends on the resolution, polarisation, SCR, target amplitude distribution and clutter distribution. This section discusses the influence of vertically or horizontally polarised sea clutter on the detection performance, based on sea clutter collected by the Ingara radar system.

The polarisation index (PI) is defined as the ratio of the HH backscattering coefficient σ_{hh}^0 to the VV backscattering coefficient σ_{vv}^0. If the Bragg scattering mechanism dominates sea clutter at high incidence angles, the PI is simplified to the ratio of the Bragg scattering coefficients, as

$$\beta = \left|\alpha_{hh} / \alpha_{vv}\right|^2 \tag{19}$$

where the Bragg scattering coefficients are given by (Elachi, 1987),

$$\alpha_{hh} = \frac{\varepsilon_r - 1}{\left(\cos\theta + \sqrt{\varepsilon_r - \sin^2\theta}\right)^2} \tag{20}$$

$$\alpha_{vv} = \left(\varepsilon_r - 1\right)\frac{\varepsilon_r\left(\sin^2\theta + 1\right) - \sin^2\theta}{\left(\varepsilon_r\cos\theta + \sqrt{\varepsilon_r - \sin^2\theta}\right)^2} \tag{21}$$

where θ is the incidence angle (the incidence angle and the grazing angle are complementary angles) and ε_r is the dielectric constant of seawater. Given $\varepsilon_r = 65 - j40$ for seawater at X-band (Holliday et, al, 1998), and an incidence angle of 50°, we calculate the PI according to (19) to be −10dB. That is, the mean of the HH sea clutter should be 10dB lower than the mean of VV sea clutter should the Bragg scatterers be only the scatterers in the sea clutter at the incidence angle of 50°. The cdfs of the HH and VV sea clutter of run34690_225 (upwind) and run34690_075 (downwind) are shown in Figure 26 and Figure 27, respectively. It is seen that in the region of $0 < cdf < 0.999$, the HH amplitude is consistently about 5 to 8 dB lower than the VV amplitude for the same cdf level. On the other hand, it is reasonable to assume that the RCS of a man-made target is approximately the same for the HH and VV polarisations. Therefore, we conclude that at a high grazing angle, the HH polarisation outperforms the VV polarisation for target detection. In the higher tail region of $cdf > 0.9999$, the cdf difference between the two polarisations gradually disappears due to the spikier nature of the HH sea clutter.

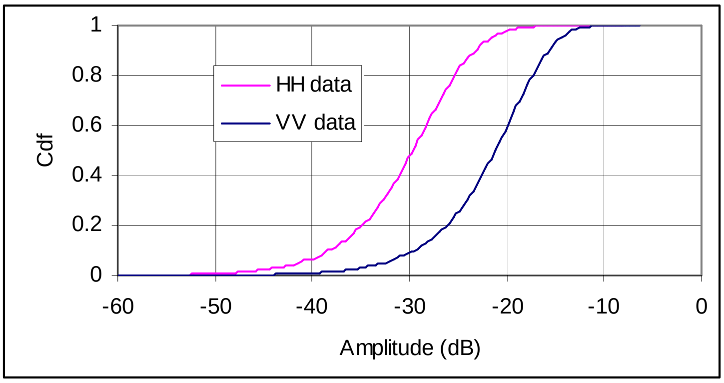

(a) cdf abscissa on linear scale

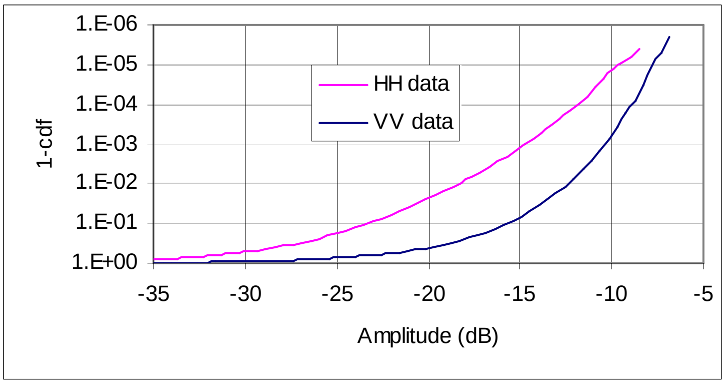

(b) cdf abscissa on log scale

Figure 26: Cdfs of the HH and VV sea clutter of run34690_225 (upwind).

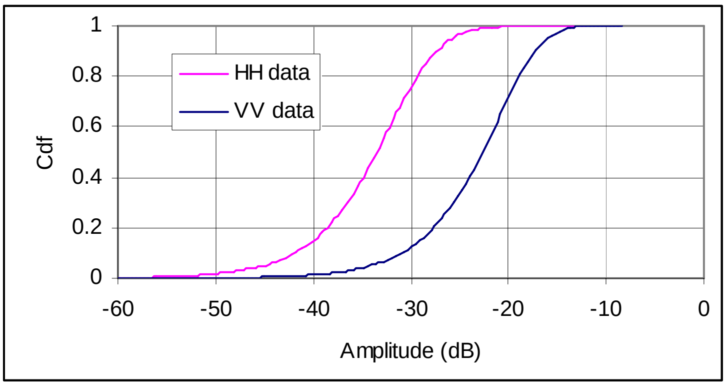

(a) cdf abscissa on linear scale

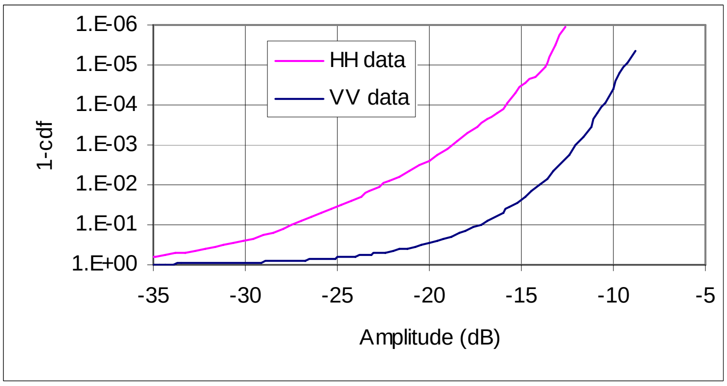

(b) cdf abscissa on log scale

Figure 27: Cdfs of the HH and VV sea clutter of run34690_075 (downwind).

Watts' calculation (1996b) indicates that a vertically polarised radar performs better than a horizontally polarised radar if the grazing angle is less than about 4^{o}. This angle is referred to as a critical angle. Above this critical angle, a horizontally polarised radar performs better. The above high grazing angle sea clutter analysis seems to be consistent with this claim.

According to the Ingara measurement, the cross-polarised HV amplitude is consistently further 7 to 10 dB lower than the HH amplitude at the same cdf level. However, unless the cross-polarised RCS of man-made targets is fully investigated, we cannot conclude whether the cross-polarised mode outperforms/underperforms the co-polarised mode (refer to Section 4 for further discussions).

According to the observation of Lee et al (1996), the ratio of the mean HH clutter to the mean VV clutter dramatically increases with respect to an increase in wind velocity at a grazing angle of 10^{o}. Whether this is the case for much higher grazing angle and whether the ratio will exceed 0dB at greater wind velocities are not known, but would be interesting to find out in the future.

3.2 Entropy-Alpha Decomposition

The Entropy-Alpha decomposition of polarimetric radar data proposed by Cloude and Pottier (1997) has been widely used for classification applications. Theoretically, different scattering mechanisms have different values of entropy, H, and alpha, $\overline{\alpha}$, and therefore, can be discriminated. In this section we look at the Entropy-Alpha decomposition of sea clutter, which often helps to understand scattering mechanisms involved in sea clutter, and more importantly see if such decomposition can assist in separating the target from clutter.

An incident or scattered wave may be expressed as a combination of a pair of orthogonal waves perpendicular to the propagation direction. The scattered wave is linked to the incident wave via the scattering matrix by (Ulaby and Elachi, 1990),

$$\mathbf{e}^s = \frac{e^{jkr}}{r}\mathbf{S}\mathbf{e}^i \tag{22}$$

where r is the distance between the scatterer and the antenna, k is the wave number, $\mathbf{e}^s$ and $\mathbf{e}^i$ are the scattered and incident waves, respectively. The scattered wave may be decomposed into the horizontally and vertically polarised components and (22) may be written in an explicit form as,

$$\begin{bmatrix} e_h^s \\ e_v^s \end{bmatrix} = \frac{e^{jkr}}{r}\begin{bmatrix} s_{hh} & s_{vh} \\ s_{hv} & s_{vv} \end{bmatrix}\begin{bmatrix} e_h^i \\ e_v^i \end{bmatrix} \tag{23}$$

Different scattering mechanisms exhibit different polarimetric properties determined by their scattering matrices. The polarimetric decomposition estimates the average scattering mechanism based on the decomposition of the matrix $\langle \mathbf{T} \rangle$, given by,

$$\langle \mathbf{T} \rangle = \frac{1}{N}\sum_{k=1}^{N} \mathbf{t}_k \mathbf{t}_k{}^H \tag{24}$$

where the superscript H denotes Hermitian transpose, and $\mathbf{t}$ is the scattering vector formed from the scattering matrix as,

$$\mathbf{t} = \frac{1}{2}\left[s_{hh} + s_{vv} \quad s_{hh} - s_{vv} \quad s_{hv} + s_{vh}\right]^T \tag{25}$$

where the superscript T denotes transpose, and s_{ij} $i, j = h$ or v, are elements of the scattering matrix, and $s_{hv} = s_{vh}$ under the backscattering condition.

The eigenvector decomposition of $\langle \mathbf{T} \rangle$ is expressed as,

$$\langle \mathbf{T} \rangle = \mathbf{U} \begin{bmatrix} \lambda_1 & 0 & 0 \\ 0 & \lambda_2 & 0 \\ 0 & 0 & \lambda_3 \end{bmatrix} \mathbf{U}^H \tag{26}$$

The unitary eigenvector matrix $\mathbf{U}$ is written as,

$$\mathbf{U} = \begin{bmatrix} \cos\alpha_1 & \cos\alpha_2 & \cos\alpha_3 \\ \sin\alpha_1 \cos\beta_1 e^{j\delta_1} & \sin\alpha_2 \cos\beta_2 e^{j\delta_2} & \sin\alpha_3 \cos\beta_3 e^{j\delta_3} \\ \sin\alpha_1 \sin\beta_1 e^{j\gamma_1} & \sin\alpha_2 \sin\beta_2 e^{j\gamma_2} & \sin\alpha_3 s \sin\beta_3 e^{j\gamma_3} \end{bmatrix} \tag{27}$$

In general, the above 3-by-3 unitary eigenvector matrix has only eight independent parameters since the columns are not only unitary but mutually orthogonal. This means that in practice not all α_i, β_i, γ_i and δ_i, $i = 1, 2, 3$, are independent (Cloude and Pottier, 1997).

Three eigenvalues may represent the amplitudes of three different scattering mechanisms, and the probability of the each scattering mechanism is defined by,

$$P_i = \frac{\lambda_i}{\Sigma_{k=1}^{3} \lambda_k} \tag{28}$$

The entropy H is given by,

$$H = \sum_{i=1}^{3} - P_i \log_3 P_i \tag{29}$$

The range of entropy is therefore $0 \le H \le 1$. Another main parameter for identifying the dominant scattering mechanism is the mean alpha angle,

$$\overline{\alpha} = \sum_{i=1}^{3} P_i \alpha_i \tag{30}$$

The range of $\overline{\alpha}$ is therefore $0 \le \overline{\alpha} \le 90^o$. The classification space of the Entropy-Alpha decomposition given by Cloude and Pottier (1997) is redrawn in Figure 28 for reference.

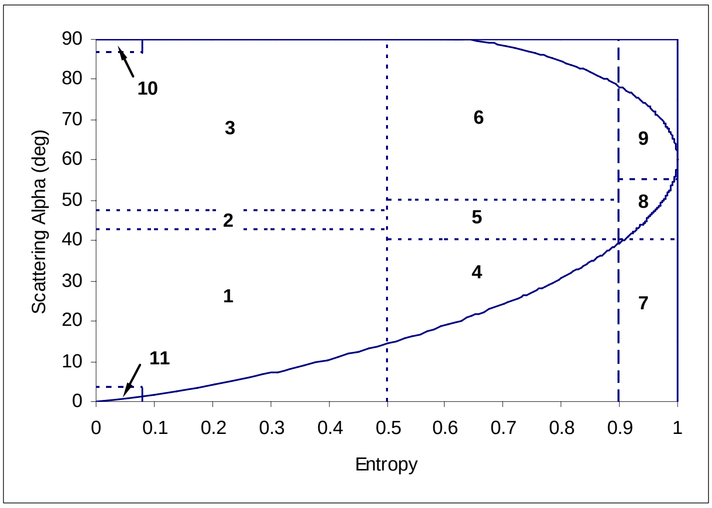

Figure 28: Entropy-Alpha classification space: 1 – low entropy surface scattering, 2 – low entropy dipole scattering, 3 – low entropy multiple scattering, 4 – medium entropy surface scattering, 5 – medium entropy vegetation scattering, 6 – medium entropy multiple scattering, 7 – high entropy surface scattering, 8 – high entropy vegetation scattering, 9 – high entropy multiple scattering, 10 – dihedral scattering and 11 – trihedral scattering.

The Cloude-Pottier Entropy-Alpha decomposition of the sea clutter dataset, run34683_225 (upwind) is shown in Figure 29 (a) and (b) using 3 and 9 range samples, respectively, for estimation of the matrix $\langle \mathbf{T} \rangle$. It can be seen that the dominant entropy increases slightly with an increase in the number of range samples used in the estimation of the scattering matrix. This is understandable, as the more samples used in the average, the less differences among the three eigenvalues and hence larger the entropy. The dominant scattering mechanism for this sea clutter dataset, according to the classification zones given by Cloude and Pottier (1997), is the low entropy surface scattering, i.e., the Bragg surface scattering. However, other scattering mechanisms also exist, including low entropy dipole scattering (a large imbalance between HH and VV in amplitude), low entropy multiple scattering and medium entropy scattering. In conclusion, the composition of sea surface is complex and contains a variety of scatterers. The spread of the distribution of sea clutter data in the Entropy-Alpha plane therefore covers a large portion of the feasible area.

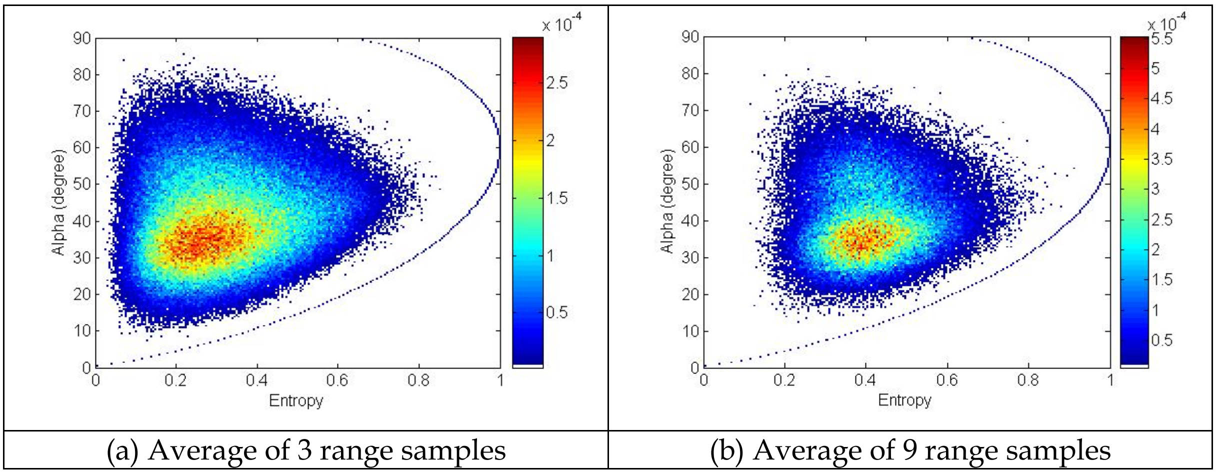

(a) Average of 3 range samples

(b) Average of 9 range samples

Figure 29: Distribution of the Entropy-Alpha decomposition of the sea clutter of dataset run34683_225 with (a) 3 range samples and (b) 9 range samples being used for estimation of the matrix $\langle \mathbf{T} \rangle$*. The curved line bounds the feasible area of the decomposition.*

To examine the scattering mechanisms involved in sea spikes, the Entropy-Alpha decomposition of sea spikes is shown in Figure 30. The process first locates spikes using a cell-average constant false-alarm rate (CA-CFAR) scheme with a CA window of 24 range cells and a false-alarm rate of $P_{fa} = 10^{-4}$. Each of the located spikes with its fore and aft range cells are then used in the estimation of the matrix $\langle \mathbf{T} \rangle$, and its Entropy-Alpha decomposition is computed. It can be seen from the figure that the VV sea spikes are usually low entropy surface scatterers. The low entropy of the VV spikes indicates that in general only one scatterer is dominant in the VV spikes. On the other hand, the entropy of the HH spikes is spread, indicating that more than one scatterer contributes to the HH spikes, and thus the form of the HH spikes are more complex than the form of the VV spikes.

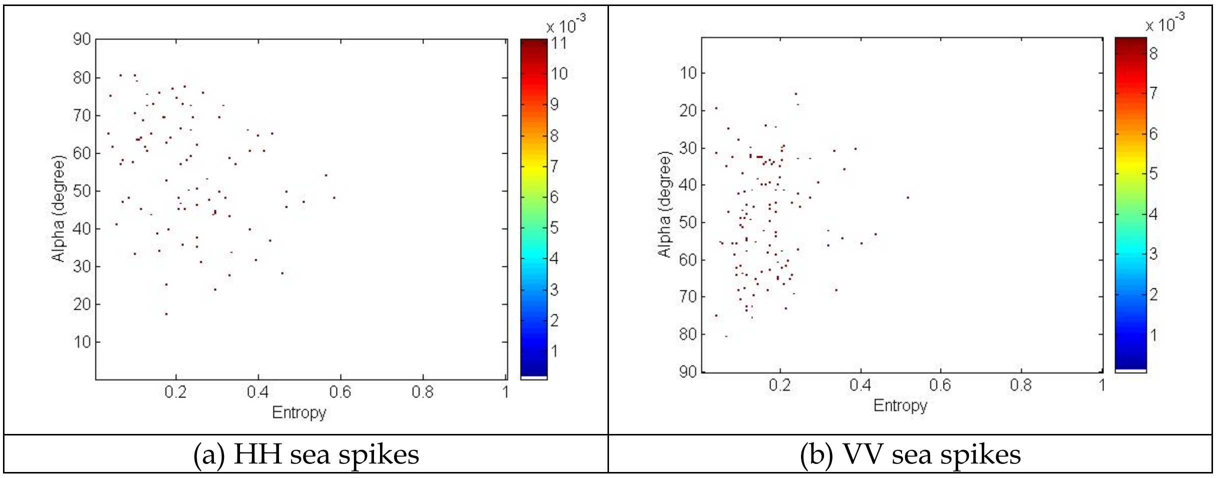

(a) HH sea spikes

(b) VV sea spikes

Figure 30: The Entropy-Alpha decomposition of sea spikes in the (a) HH and (b) VV datasets of run34683_225. The false-alarm rate was set to $P_{fa} = 10^{-4}$*.*

4. Polarisation Analysis for Target Detection

We have studied polarisation characteristics of sea clutter using the real aperture X-band radar data collected by the Ingara system. We now turn our intention to the characteristics of targets. In doing so, a C-band polarimetric SAR dataset collected by the NASA/JPL AirSAR system is re-examined in this report, as the dataset contains small sea surface targets, typically, wooden fishing vessels. Polarisation signatures of typical scattering mechanisms are first reviewed to help understand responses of targets in the dataset and searching for the best polarisations which maximally discriminate target response from sea clutter.

4.1 Polarisation Signatures of Common Scattering Mechanisms

Different scattering mechanisms exhibit different polarimetric properties determined by their scattering matrices. This section investigates polarisation responses of different scattering mechanisms. The polarisation which maximises the ratio of target response to clutter response would be the optimum polarisation for target detection.

Polarisation signatures visually depict the response of every possibly realisable polarisation mode for a scattering mechanism. Polarisation signatures can be constructed from the Mueller matrix which in turn is formed from the scattering matrix defined by (23). Details of polarisation signatures can be found elsewhere (Ulaby and Elachi, 1990, Morris, 2004), and are skipped in this report.

Apart from the HH, VV and HV polarisations, we are also interested in other polarisations including RR (right-hand circular transmit and right-hand circular receive), LL (left-hand circular transmit and left-hand receive), RL, LR, co-slant 45° and cross-slant 45°. The axis of slant 45° polarisation $\hat{s}$ may be realised by rotating either the axis of the H polarisation $\hat{h}$ 45°, or the axis of the V polarisation $\hat{v}$ -45° as shown in Figure 31. Alternatively, the slant 45° polarisation can be synthesised using a combination of the H and V polarisations, i.e., $\hat{s} = (\hat{h} + \hat{v}) / \sqrt{2}$.

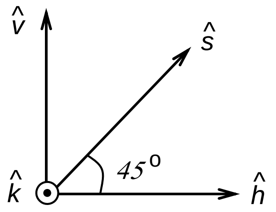

Figure 31: Slant 45° polarisation $\hat{s}$ may be realised by rotating either the $\hat{h}$ polarisation 45° or the $\hat{v}$ polarisation -45°. Alternatively, the slant polarisation can be synthesised using a combination of the H and V polarisations. The unit vector $\hat{k}$ is the propagation direction, and $\hat{h}$, $\hat{v}$ and $\hat{k}$ comprise the right-handed orthogonal coordinate system $(\hat{h}, \hat{v}, \hat{k})$.

Figure 32 shows the polarisation signatures of the odd-bounce scattering mechanism, such as a large conducting sphere or a large conducting trihedral corner reflector. The responses of the polarisations of interests are also marked.

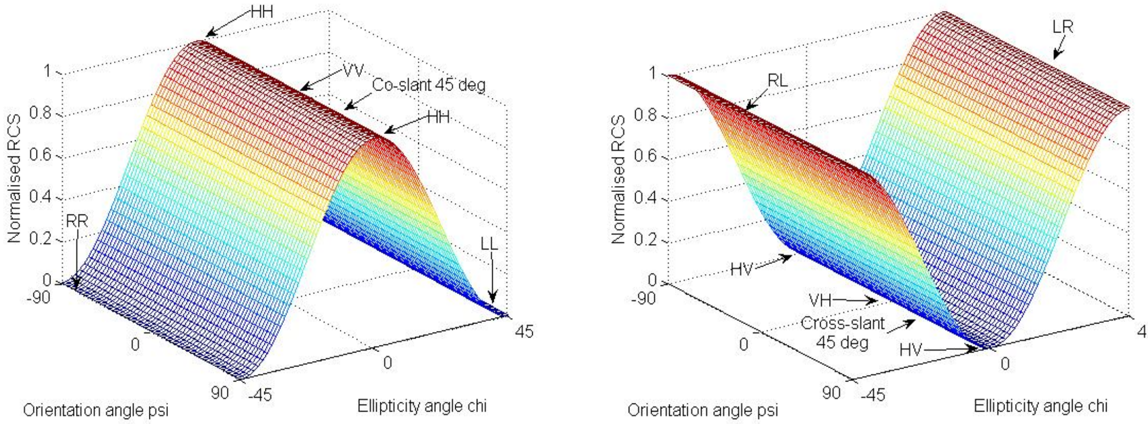

(a) co-polarisation response (b)cross-polarisation response

Figure 32: Polarisation signatures of the odd-bounce scattering mechanism, such as a large conducting sphere, or a large conducting trihedral corner reflector.

The Bragg scattering is often dominant in sea clutter. Using the Bragg scattering coefficients given in (20)-(21), we show in Figure 33 the polarisation signatures of the Bragg scattering mechanism with parameters of an incidence angle $\theta = 50^o$ and a dielectric constant $\varepsilon_r = 65 - j40$ (the dielectric constant of seawater at X-band or C-band).

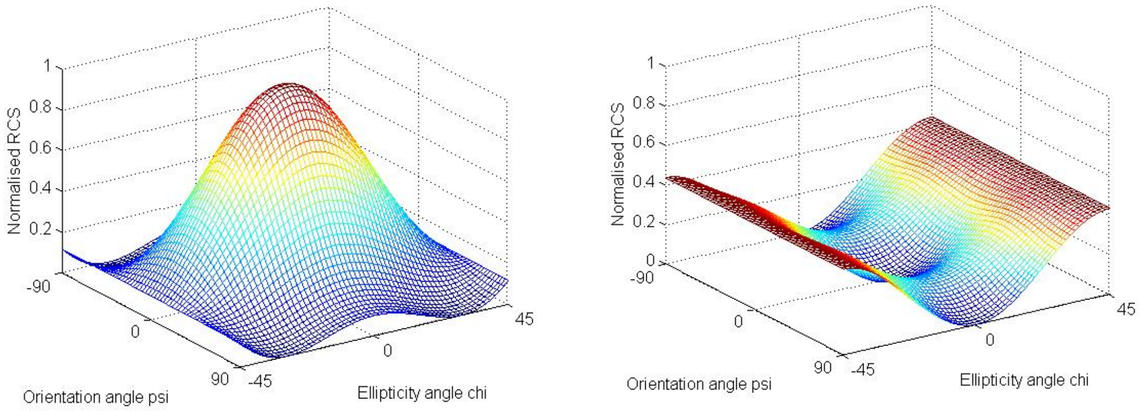

(a) co-polarisation response (b)cross-polarisation response

Figure 33: Polarisation signatures of the Bragg scattering mechanism with parameters of an incidence angle $\theta = 50^o$ and a dielectric constant $\varepsilon_r = 65 - j40$ (the dielectric constant of seawater at X-band or C-band).

The polarisation signatures of the even-bounce scattering mechanism, such as a large conducting dihedral corner reflector, are shown in Figure 34.

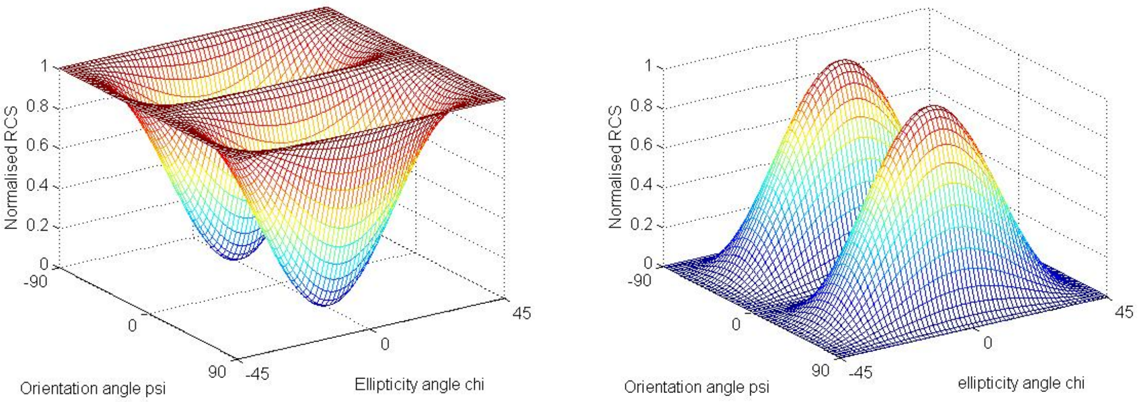

(a) co-polarisation response (b)cross-polarisation response

Figure 34: Polarisation signatures of the even-bounce scattering mechanism, such as a large conducting dihedral corner reflector.

Structures of large conducting left- and right-handed helixes are shown in Figure 35, and their polarisation signatures are shown in Figure 36 and Figure 37, respectively.

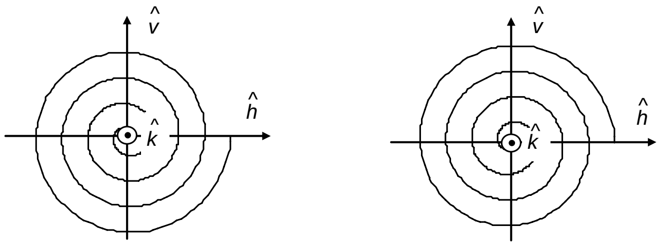

Figure 35: Large conducting left- and right-handed helixes.

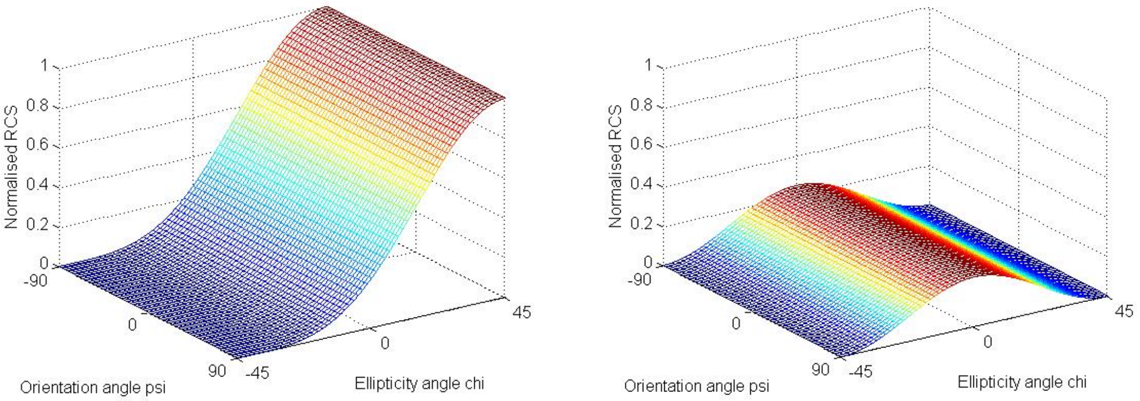

(a) co-polarisation response (b)cross-polarisation response

Figure 36: Polarisation signatures of a large conducting left-handed helix.

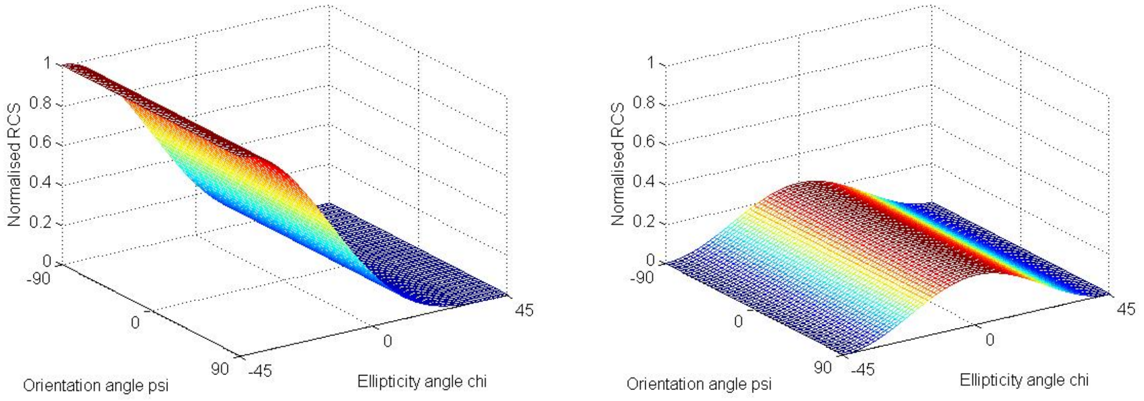

(a) co-polarisation response (b)cross-polarisation response

Figure 37: Polarisation signatures of a large conducting right-handed helix.

The polarisation responses of the above four scattering mechanisms are summarised in Table 5. The maximum RCS of each mechanism is normalised to unity. It can be seen that even for such simple scattering mechanisms, no single polarisation is perfect in terms of detecting all target signals (odd, even and helices) while suppressing clutter (Bragg). For instance, the HH polarisation can maximally suppress clutter (Bragg scattering) and maximally detect the odd- and even-bounce scatterers, but it also suppresses responses of the left- and right-handed helices. On the other hand, different polarisations may help to detect targets with particular scattering mechanisms. For instance, the cross-slant 45° polarisation detects even-bounce scatterers but suppresses all the other three scatterers and sea clutter. If we assume that the Bragg scattering is dominant in sea clutter and the returns of targets are dominated by the even- and odd-bounce scattering mechanisms, then the HH polarisation shall perform the best.

Table 5: Typical scattering mechanisms and their polarisation responses

Scattering Mechanism	**Polarisation & Response**						
	HH	VV	HV	RR/LL	RL/LR	Slant 45° co-pol	slant 45° cross-pol
Bragg	0.1	1	0	0.12	0.43	0.43	0.12
Odd	1	1	0	0	1	1	0
Even	1	1	0	1	0	0	1
Right/left-hand helix	0.25	0.25	0.25	1	0	0.25	0.25

4.2 Re-examination of AirSAR Data

The NASA/JPL AirSAR P-, L- and C-band data over the Darwin harbour were collected on November 23rd 1996. The collection commenced at about 9:15am and finished at 11:45am local time. Located at Frances bay, Fannie Bay and Sadgroves Creek, respectively, three groups of anchored vessels were used as test targets. The wind speed was about 3.5-4.2m/s on the day. Details of this trial and analysis of the SAR data were reported elsewhere (Dong and Forster, 1998). This section re-examines C-band data, as the frequency of C-band is closest to the frequency of X-band.

Figure 38 shows the C-band SAR images of the Darwin Harbour, and locations of the three groups of test vessels are also marked. The SAR data was multi-look processed and re-sampled into a ground resolution of approximate $9.26 \times 9.26\,\mathrm{m}^2$ per pixel. A brief summary of the radar observation of the three groups of test vessels is given in Table 6. Test vessels in Group I and II were controlled and anchored and their locations were recorded using a GPS device. The sizes and materials of these vessels were also recorded and the vessels themselves were photographed. Table 7 and Table 8 provide general descriptions of test vessels in Groups I and II, respectively. The vessels of Group III, on the other hand, were not controlled, and they were only GPS readings of anchored private vessels in the creek taking about two hours prior to the SAR data collection commencing.

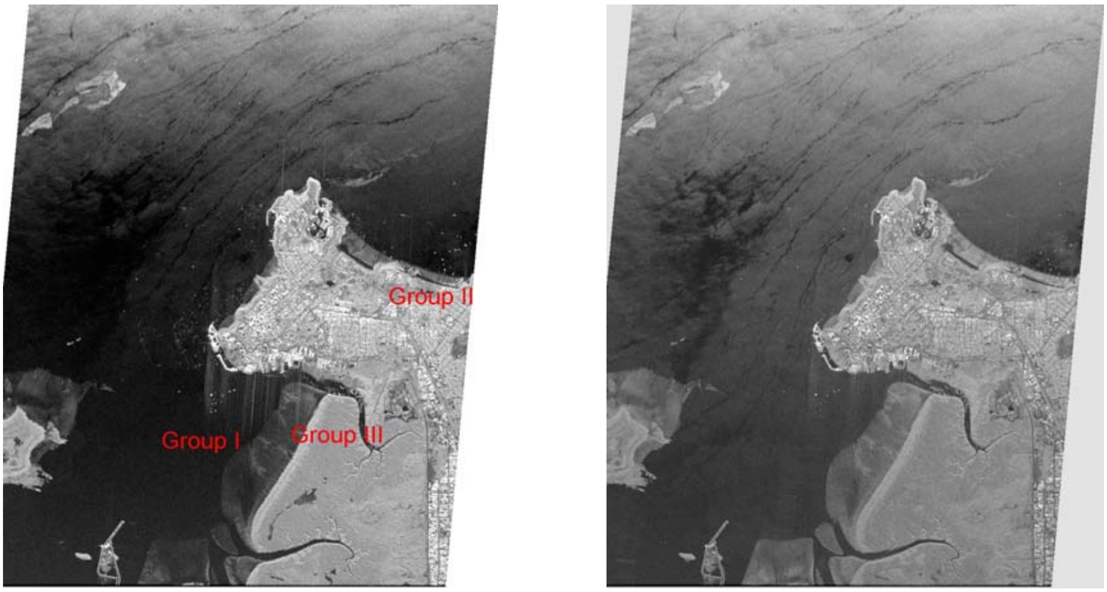

(a) HH (b) VV

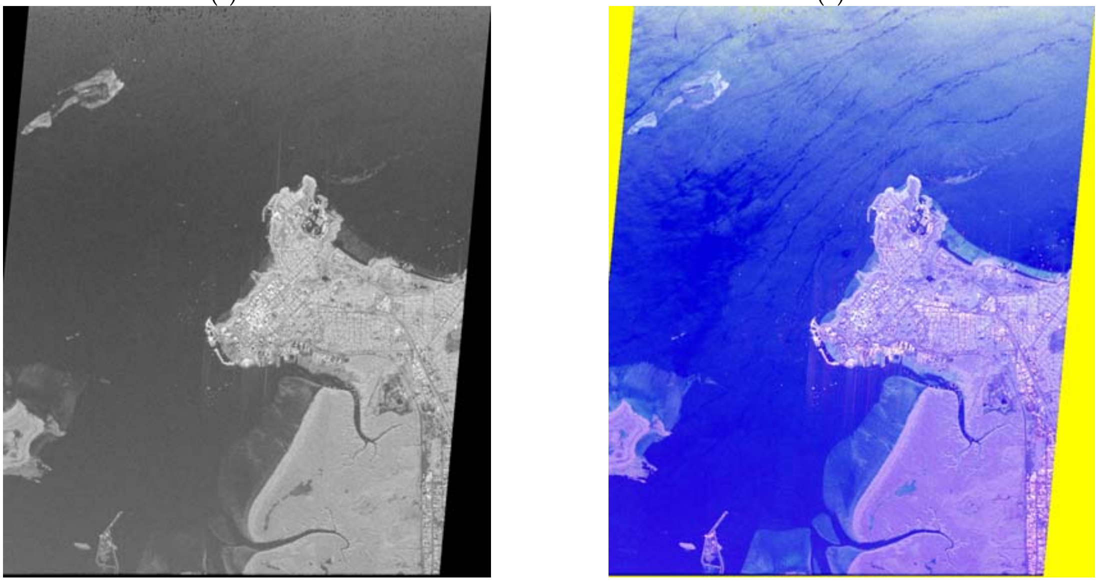

(c) HV (d) colour composite, R:HH, G:VV and B:HV

Figure 38: NASA/JPL AirSAR C-band image of Darwin Harbour. Locations of three groups of small vessels are marked. The image contains 1092 pixels in azimuth (approximately in horizontal) and 1291 pixels in range (approximately in vertical), and covers an approximately $10.11 \times 11.95\, km^2$ *on the ground.*

Table 6: A brief summary of the radar observation of three groups of vessels

Group	Incidence angle (°)	No of recorded vessels	No of observed point targets
I	48	15	>15
II	36	15	>15
III	47	33	>33

Table 7: General descriptions of vessels in Group I

No	Description	Length (m)	Head orientation (°)
1	Wooden/steel frame	10	140
2	Kim B1, pearing logger, wood	12	80
3	Steel fishing boat	10	60
4	Wooden fishing boat	15	120
5	Barefoot Venture, steel	12	140
6	Wooden fishing boat	20	140
7	Wooden fishing boat	15	160
8	Wooden fishing boat	15	160
9	Wooden fishing boat	15	160
10	Wooden fishing boat	20	140
11	Wooden fishing boat	15	140
12	Wooden fishing boat	10	140
13	Wooden fishing boat	15	140
14	Wooden fishing boat	15	130
15	Wooden fishing boat	15	145

Table 8: general description of vessels in Group II

No	Description	Length (m)	Head orientation (°)
1	Broadreach fibreglass yacht	8	160
2	Torres Voyager II Mast wooden yacht	8	170
3	Born Free aluminium dinghy	10	200
4	Mistres Cabin Cruiser, wooden/fibre	7	215
5	Little Mat, aluminium	10	180
6	R'N'R Darwin, fibreglass	8	120
7	Ethos, aluminium	12	140
8	Farr 5000, fibreglass	5	135
9	Dove, fibreglass	6	165
10	Salamander fibreglass yacht	8	180
11	Kiri Kanan Trimerran, fibreglass	14	170
12	Fibreglass yacht	7	185
13	Midnight Special yacht, fibreglass	5	185
14	Fibreglass yacht	5	215
15	Lorian yacht, fibreglass	5	165

Orientation of vessels in Table 7 and Table 8 is defined as follows. If the bow of a vessel is towards the north, the orientation is 0^o, east, 90^o, south, 180^o and so on. Since the aircraft flew approximately from north to south, and the radar looked to east, vessels having approximately 0^o or 180^o orientation should be seen at the broadside aspect angles.

The zoomed-in images containing the three groups of vessels are shown in Figure 39, Figure 40 and Figure 41, respectively. It is seen that the number of the observed point targets are about one or two more than the number of recorded vessels in Groups I and II. One possible explanation is that some vessels sailed into the test areas during the data collection. In the case of Group III, the number of observed point targets is significantly more than the recorded. Since the creek was not controlled, many private vessels could be expected to come and go on a summer Saturday morning.

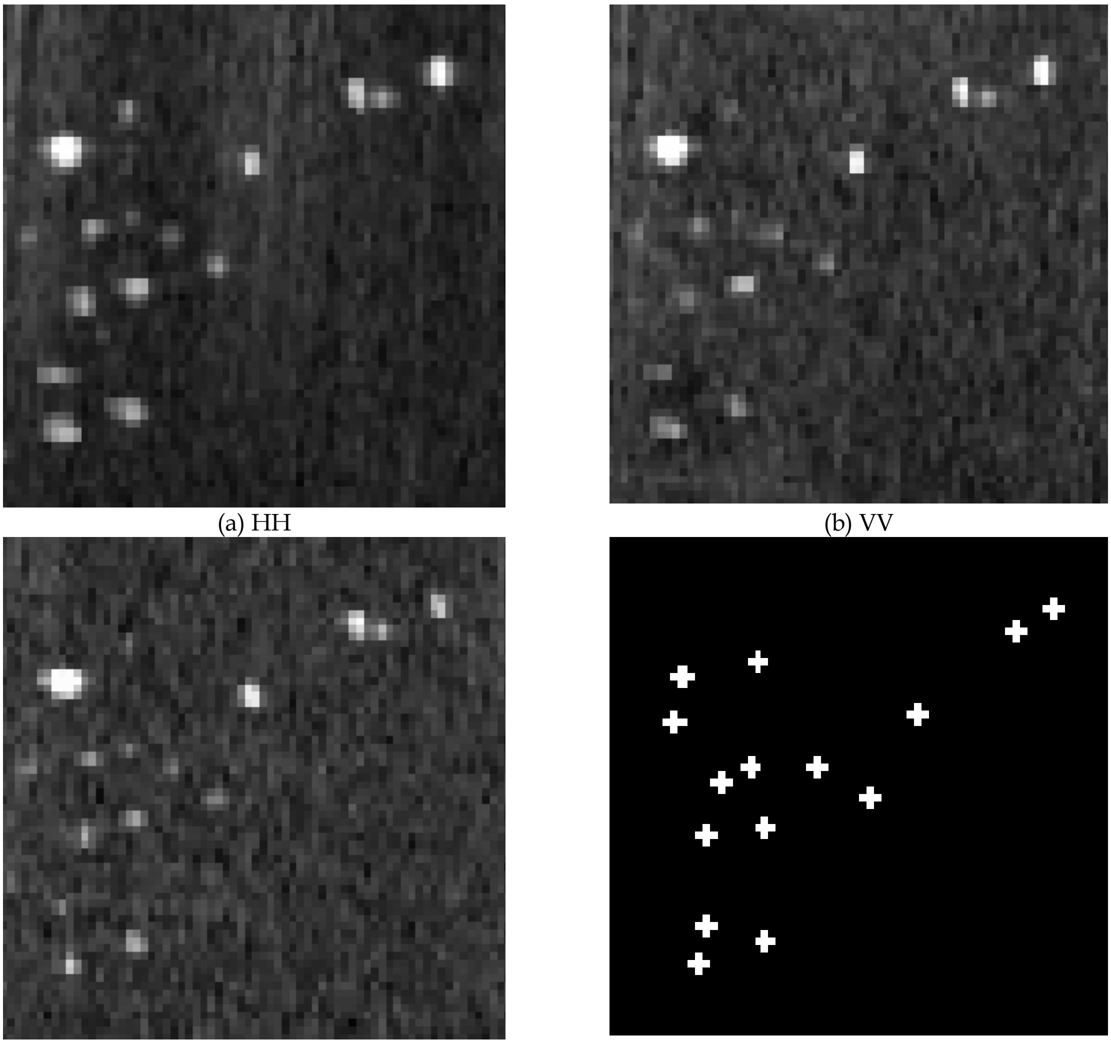

(a) HH

(b) VV

(c) HV

(d) Recorded coordinates of test vessels

Figure 39: The zoomed-in (a) HH, (b) VV and (c) HV images containing vessels of Group I. The correspondingly recorded vessel positions are shown in (d). A total of 15 vessels were recorded in Group I.

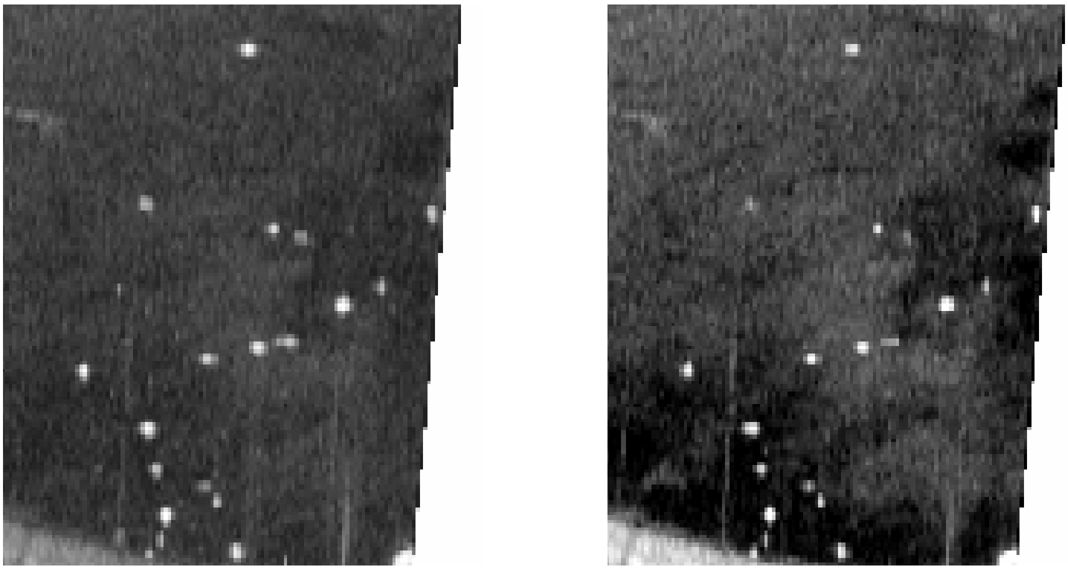

(a) HH (b) VV

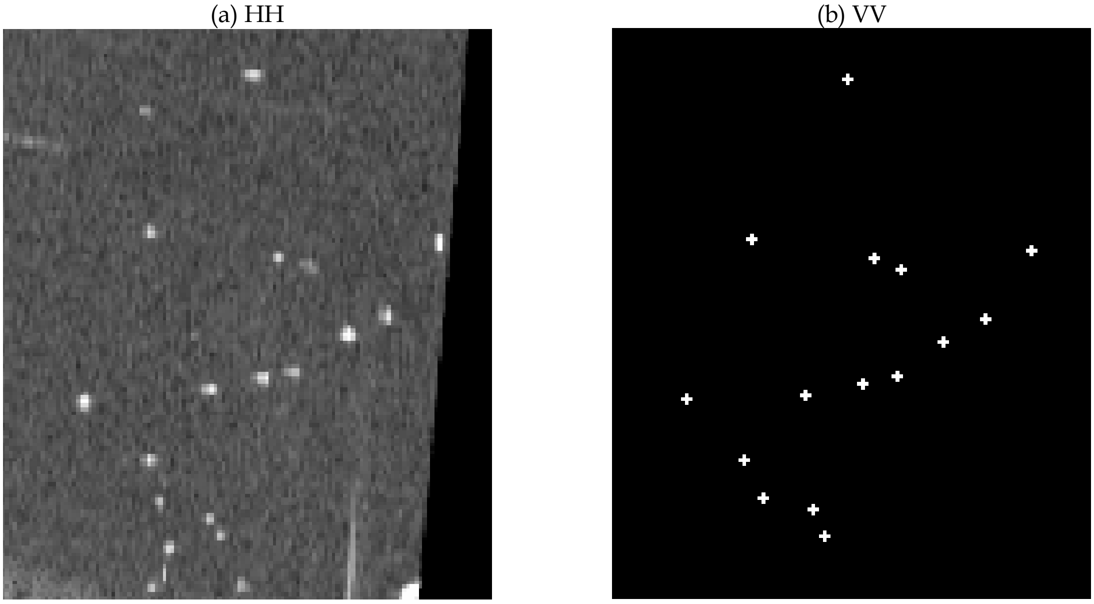

(c) HV (d) Recorded coordinates of test vessels

Figure 40: The zoomed-in (a) HH, (b) VV and (c) HV images containing vessels of Group II. The correspondingly recorded vessel positions are shown in (d). A total of 15 vessels were recorded in Group II.

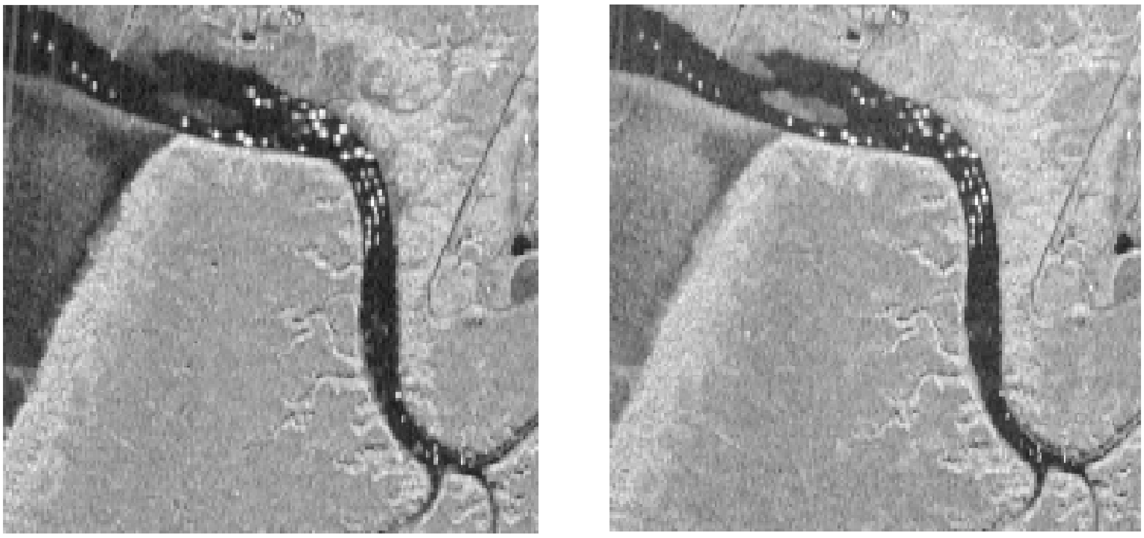

(a) HH (b) VV

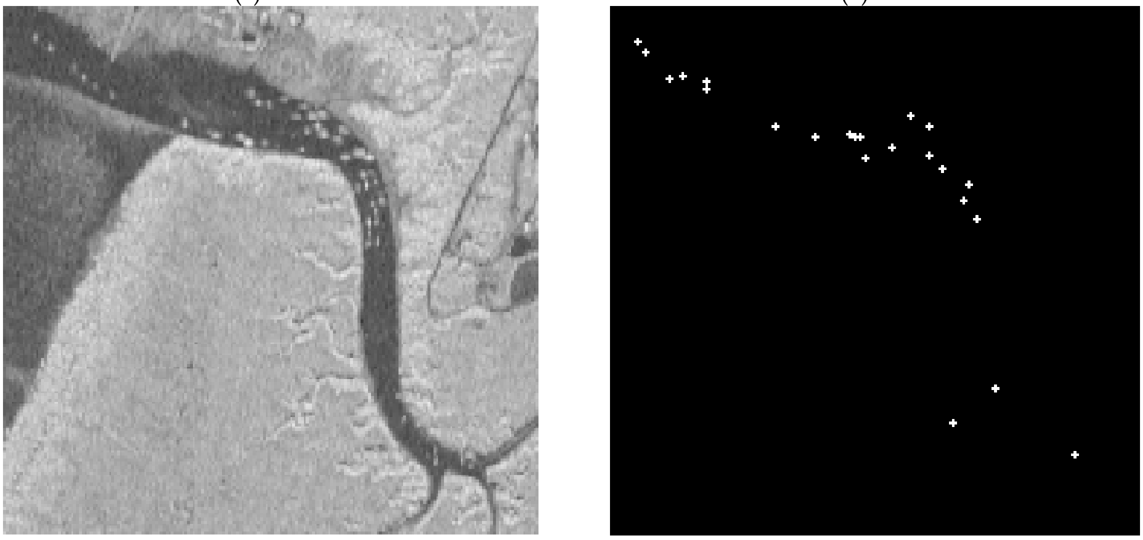

(c) HV (d) Recorded coordinates of test vessels

Figure 41: The zoomed-in (a) HH, (b) VV and (c) HV images containing vessels of Group III. The correspondingly recorded vessel positions are shown in (d). A total of 33 vessels were recorded in Group III, but only 22 vessel positions are shown in (d), as some of their coordinates are too close to be discriminated.

The vessel identifiers, i.e., the numbers, associated with their relative coordinates for Groups I and II are depicted in Figure 42. Metal vessels, such as number 5 in Group I and number 7 in Group II are much stronger scatterers than wooden and fibreglass vessels if one views Figure 39 and Figure 40.

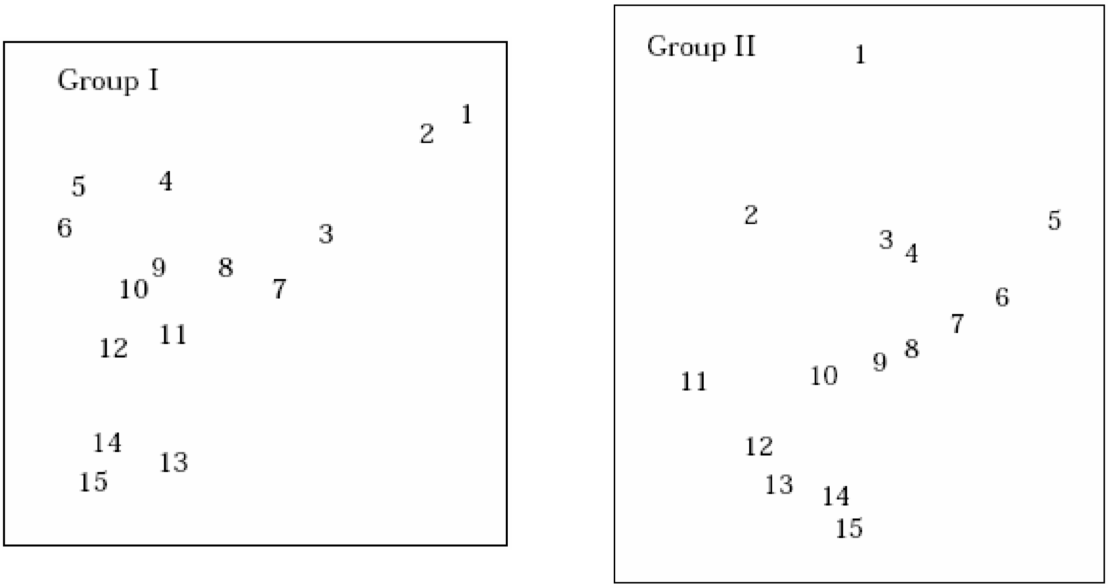

(a) Group I (b) Group II

Figure 42: Relative coordinates of vessels in Groups I and II.

Due to the nature of the SAR processing, the energy of a strong point target spreads into its neighbouring pixels. The RCS of a vessel may be calculated by an incoherent summation of the spread energies. The measured RCS of a SAR-imaged target is calculated as the pixel area times the difference of a summation of the backscattering coefficients of the target pixel and its neighbouring pixels minus a summation of the backscattering coefficients of the background for the same pixels. On the other hand, to discriminate a target (vessel) from the background (sea), the difference between the target response and the sea clutter is the most important. We define the SCR of a target as following. The signal level of a target is defined as the mean backscattering coefficient of the target pixel (the brightest pixel) and its two range neighbour pixels (near and far) and two azimuth neighbour pixels (fore and aft). A nearby 30-by-30 pixels of a uniform background area is selected as the clutter, the backscattering coefficients of these 900 pixels are sorted and the mean backscattering coefficient of the top 10% of the block (e.g., the 90 pixels with the highest backscattering coefficients) is used as the clutter level. The SCR is the ratio of the two. Shown in Figure 43 and Figure 44 are the measured HH signal and clutter levels for Groups I and II, respectively.

To qualitatively assess scattering mechanisms involved in target backscatter, one can examine the polarisation phase difference, defined as the phase difference between the HH and VV polarisations. It is well known that a double bounce scattering from a dihedral-corner-reflector like mechanism has a phase difference of about 180° whereas a odd bounce scattering from a rough surface or a trihedral-corner-reflector like mechanism experience a phase difference about 0°. The phase differences for the targets and sea clutter are also shown in Figure 43 and Figure 44.

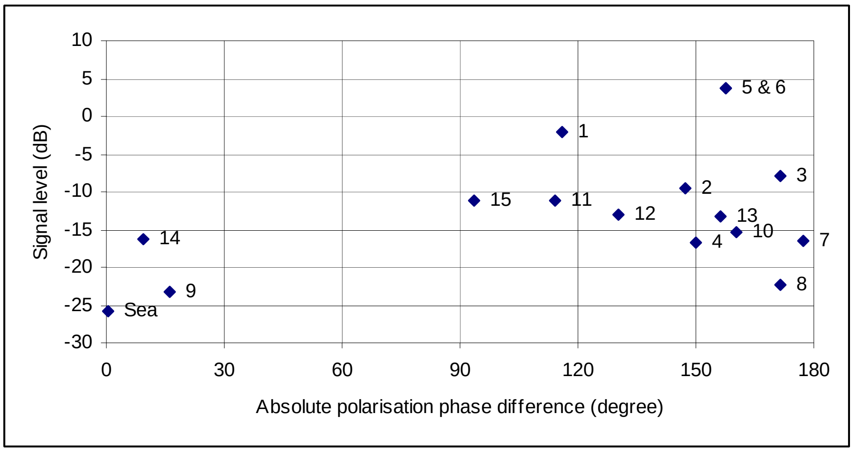

Figure 43: Measured C-band HH sea clutter and target signal levels as well as their polarisation phase differences for vessels in Group I. The polarisation phase ranges from −180° to 180°, but only the absolute values are used in plotting.

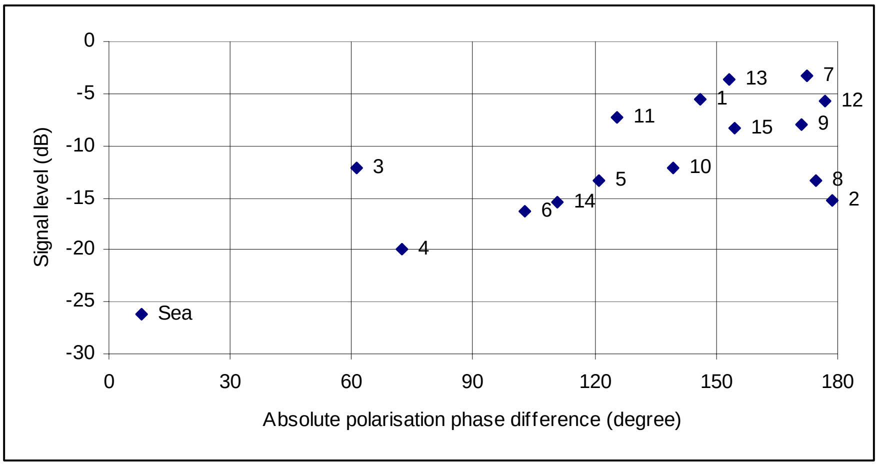

Figure 44: Measured C-band HH sea clutter and target signal levels as well as their polarisation phase differences for vessels in Group II. The polarisation phase ranges from −180° to 180°, but only the absolute values are used in plotting.

It is seen that the phase difference of the sea clutter is close to zero degrees suggesting that the dominant backscattering mechanism is the surface scattering (or more specifically, the Bragg scattering — this will become clear later). On the other hand, most target responses have a non-zero phase difference, some of them are high and close to 180°, indicating that a strong component of double bounce scattering exists in most of target responses.

4.3 Four-Component Decomposition

To separate different scattering mechanisms, the algorithm developed by Dong et al (1998) was used to decompose polarimetic data. The algorithm assumes that there are only four dominant scattering mechanisms, namely, double bounce, Bragg, odd bounce and cross scatterings. The Mueller matrix of each pixel is therefore a sum of four simple Mueller matrices representing these four scattering mechanisms, as,

$$\mathbf{F} = \sum_{i=1}^{4} \mathbf{F}_i \tag{31}$$

The explicit forms of the four Mueller matrices are given below (Dong et al, 1998).

(a) Double bounce scattering: The scattering matrix of a double bounce scattering can be written as,

$$\mathbf{S}_1 = \begin{bmatrix} s_{hh} & s_{vh} \\ s_{hv} & s_{vv} \end{bmatrix} = \begin{bmatrix} 1 & 0 \\ 0 & 1/\sqrt{\alpha}\, e^{-j\delta} \end{bmatrix} s_1 \tag{32}$$

where $s_1 = s_{hh}$ is a function of several parameters, such as the dimension, surface roughness and dielectric constant of the double bounce surfaces. α and δ are the PI and phase difference of the mechanism and can be estimated by,

$$\alpha = \left| [R_{\perp 1}(\pi - \theta) R_{\perp 2}(\theta)] / [R_{\parallel 1}(\pi/2 - \theta) R_{\parallel 2}(\theta)] \right|^2 \tag{33}$$

$$\delta = Arg\left\{ [R_{\perp 1}(\pi - \theta) R_{\perp 2}(\theta)] / [R_{\parallel 1}(\pi/2 - \theta) R_{\parallel 2}(\theta)] \right\} \tag{34}$$

where $Arg\{\cdot\}$ denotes the argument of a complex value, θ is the radar's incidence angle, $R_{\perp 1}$ and $R_{\parallel 1}$ are the horizontally and vertically polarised Fresnel reflection coefficients for the first bounce evaluated at the angle of $\pi/2 - \theta$, and $R_{\perp 2}$ and $R_{\parallel 2}$ are for the second bounce evaluated at the angle of θ. The Fresnel reflection coefficient is also a function of the dielectric constant of the reflection material. In the calculation we assume that it is the seawater saturated wooden hull and the sea surface that form the double bounce scattering mechanism, and therefore, the dielectric constant of seawater at C-band, $\varepsilon_r = 65 - j40$ was used in the calculation. The corresponding Mueller matrix is,

$$\mathbf{F}_1 = \begin{bmatrix} (\alpha+1)/2\alpha & (\alpha-1)/2\alpha & 0 & 0 \\ (\alpha-1)/2\alpha & (\alpha+1)/2\alpha & 0 & 0 \\ 0 & 0 & \cos\delta/\sqrt{\alpha} & -\sin\delta/\sqrt{\alpha} \\ 0 & 0 & -\sin\delta/\sqrt{\alpha} & -\cos\delta/\sqrt{\alpha} \end{bmatrix} s_1^2 \tag{35}$$

(b) Bragg scattering mechanism: Similar to (35), the Mueller matrix of the mechanism is,

$$\mathbf{F}_2 = \begin{bmatrix} {}^{(\beta+1)}/_{2\beta} & {}^{(\beta-1)}/_{2\beta} & 0 & 0 \\ {}^{(\beta-1)}/_{2\beta} & {}^{(\beta+1)}/_{2\beta} & 0 & 0 \\ 0 & 0 & {}^{1}/_{\sqrt{\beta}} & 0 \\ 0 & 0 & 0 & {}^{-1}/_{\sqrt{\beta}} \end{bmatrix} s_2^2 \tag{36}$$

where β is the PI value of the Bragg scattering given by (19). Obviously the phase difference of the Bragg scattering is zero degrees.

(c) Odd bounce scattering: This mechanism typically models the direct specular reflections from facets perpendicular to the incidence direction, or reflections from trihedral-corner-reflector like mechanisms. The Mueller matrix is given by,

$$\mathbf{F}_3 = \begin{bmatrix} 1 & 0 & 0 & 0 \\ 0 & 1 & 0 & 0 \\ 0 & 0 & 1 & 0 \\ 0 & 0 & 0 & -1 \end{bmatrix} s_3^2 \tag{37}$$

(d) Cross-scattering: The polarimetric response of a point target or distributed target in general can be decomposed into co-polarised and cross-polarised components. Usually the elements s_{hv} and s_{vh} of the scattering matrix $\mathbf{S}$ for an arbitrary scattering mechanism are non-zero, and reciprocity implies $s_{hv} = s_{vh}$ in the backscattering direction. In the case of a random medium, the ensemble-averaged Mueller matrix is of interest. Since the phase difference between s_{hh} and s_{vh} (or s_{vv} and s_{hv}) is uniformly distributed (Sarabandi, 1992), statistically we have $\left\langle s_{hh} s_{vh}^{*} \right\rangle = \left\langle s_{vv} s_{hv}^{*} \right\rangle = 0$ in the Mueller matrix. Therefore, first of all, only the s_{vh}^2 term is important. Secondly, the cross-polarised components from random targets are also incoherently added together, i.e., $s_{vh}^2 = \sum_{i=1}^{k} s_{vhi}^2$ when there are k randomly distributed targets. If we are only interested in the total cross-polarised component, we can assume theoretically that the total cross-polarised response is caused by a cross-scattering mechanism, whose scattering matrix is,

$$\mathbf{S}_4 = \begin{bmatrix} 0 & 1 \\ 1 & 0 \end{bmatrix} s_4 \tag{38}$$

and the corresponding Mueller matrix is,

$$\mathbf{F}_4 = \begin{bmatrix} 1 & 0 & 0 & 0 \\ 0 & -1 & 0 & 0 \\ 0 & 0 & 1 & 0 \\ 0 & 0 & 0 & 1 \end{bmatrix} s_4^2 \tag{39}$$

The total Mueller matrix is the sum of the above four Mueller matrices. This gives,

$$\begin{bmatrix} f_{11} \\ f_{12} \\ f_{22} \\ f_{33} \\ f_{34} \\ f_{44} \end{bmatrix} = \begin{bmatrix} {}^{(\alpha+1)}\!/_{2\alpha} & {}^{(\beta+1)}\!/_{2\beta} & 1 & 1 \\ {}^{(\alpha-1)}\!/_{2\alpha} & {}^{(\beta-1)}\!/_{2\beta} & 0 & 0 \\ {}^{(\alpha+1)}\!/_{2\alpha} & {}^{(\beta+1)}\!/_{2\beta} & 1 & -1 \\ {}^{\cos\delta}\!/_{\sqrt{\alpha}} & {}^{1}\!/_{\sqrt{\beta}} & 1 & 1 \\ {}^{-\sin\delta}\!/_{\sqrt{\alpha}} & 0 & 0 & 0 \\ {}^{-\cos\delta}\!/_{\sqrt{\alpha}} & {}^{-1}\!/_{\sqrt{\beta}} & -1 & 1 \end{bmatrix} \begin{bmatrix} s_1^2 \\ s_2^2 \\ s_3^2 \\ s_4^2 \end{bmatrix} \qquad s_i^2 \geq 0 \quad i = 1, \cdots, 4 \tag{40}$$

The elements on the left side of (40) are the elements of the Mueller matrix measured by a polarimetric radar system, and s_i^2, $i = 1, \cdots, 4$, are the four unknowns to be determined. Mathematically the optimal solution of the (40) is the solution of a standard non-negative least squares (NNLS) problem, and the algorithm may be found elsewhere (Lawson and Hanson, 1974).

Images of the decomposed components of double bounce, Bragg scattering and single bounce are shown in Figure 45 (the image of the cross-polarisation has been shown in Figure 38). It can be seen that urban and vegetated land areas as well as point targets such as vessels on the sea are dominated by the double bounce mechanism. Not surprisedly the Bragg scattering is primarily seen in the seawater area but not in the urban and vegetated land areas. The urban area and vegetated areas also have a significant component of single bounce scattering. In the colour composite image, when red, green and blue represent the decomposed double bounce, Bragg and odd bounce components, respectively, the sea surface is primarily in green, whereas the urban and vegetated areas as well as vessels on the sea are in purple-like reddish colours indicating red and blue to be dominant. The zoomed-in colour composite images showing vessels of Groups I and II are shown in Figure 46. For comparison, the traditional colour composite images, of which the red, green and blue represent the HH, VV and HV components, are shown in Figure 47. In general targets in Figure 46 are easier to be identified, and this conclusion is justified below.

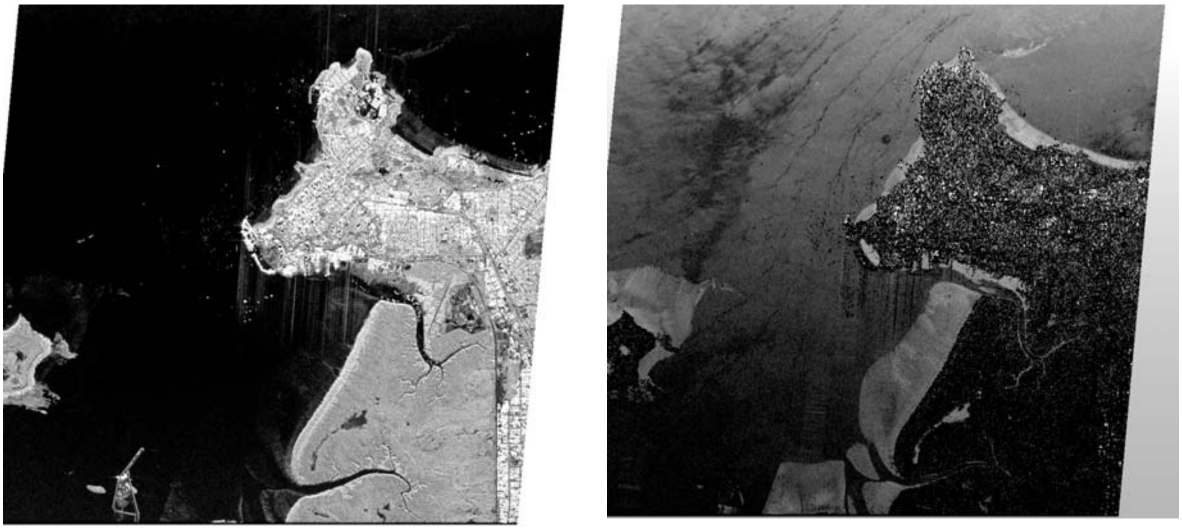

(a) Double bounce

(b) Bragg scattering

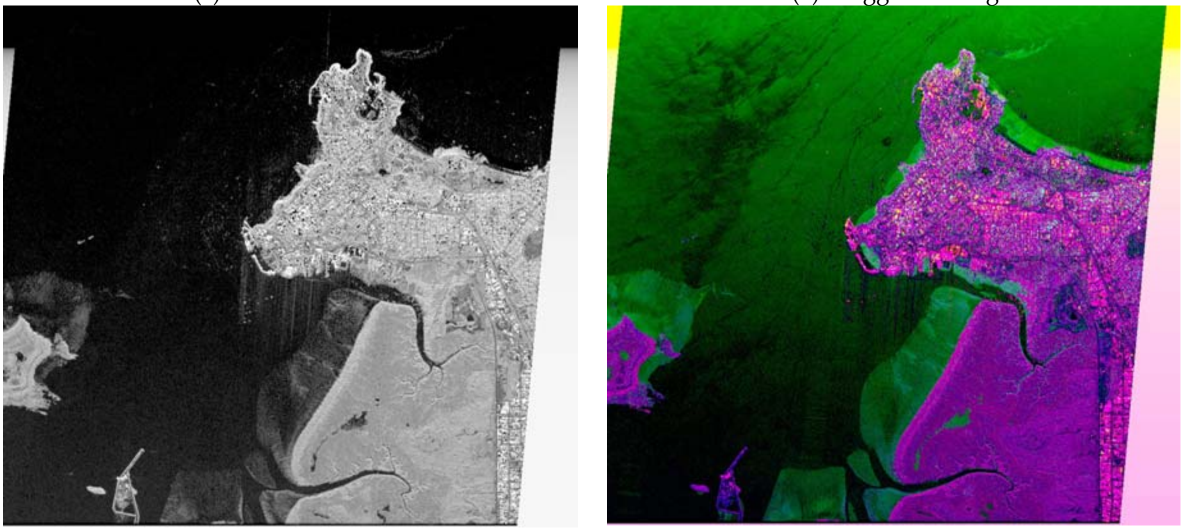

(c) Odd bounce

(d) colour composite, R: (a), G: (b) and B: (c)

Figure 45: Decomposed (a) double bounce, (b) Bragg and (c) odd bounce scattering components and (d) their colour composite images. Statistically urban and land areas including man-made objects are dominated by double and odd bounce scattering mechanisms whereas the sea surface is dominated by the Bragg scattering mechanism.

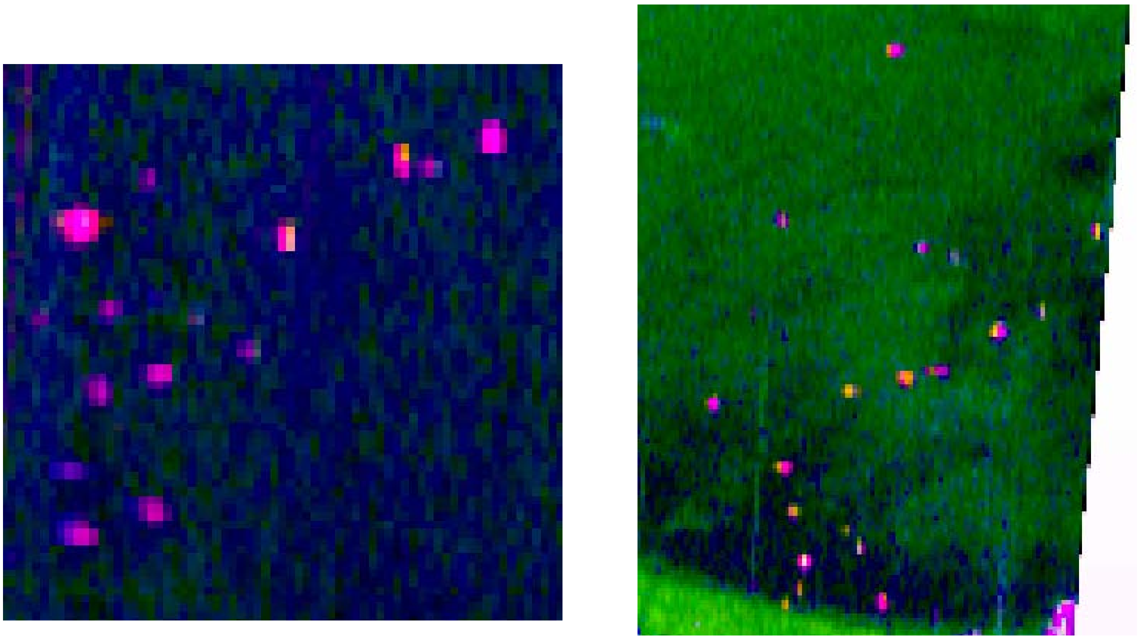

(a) Group I (b) Group II

Figure 46: Zoomed-in colour composite images showing vessels in (a) Group I and (b) Group II. The red, green and blue represent the decomposed double bounce, Bragg scattering and single bounce components, respectively.

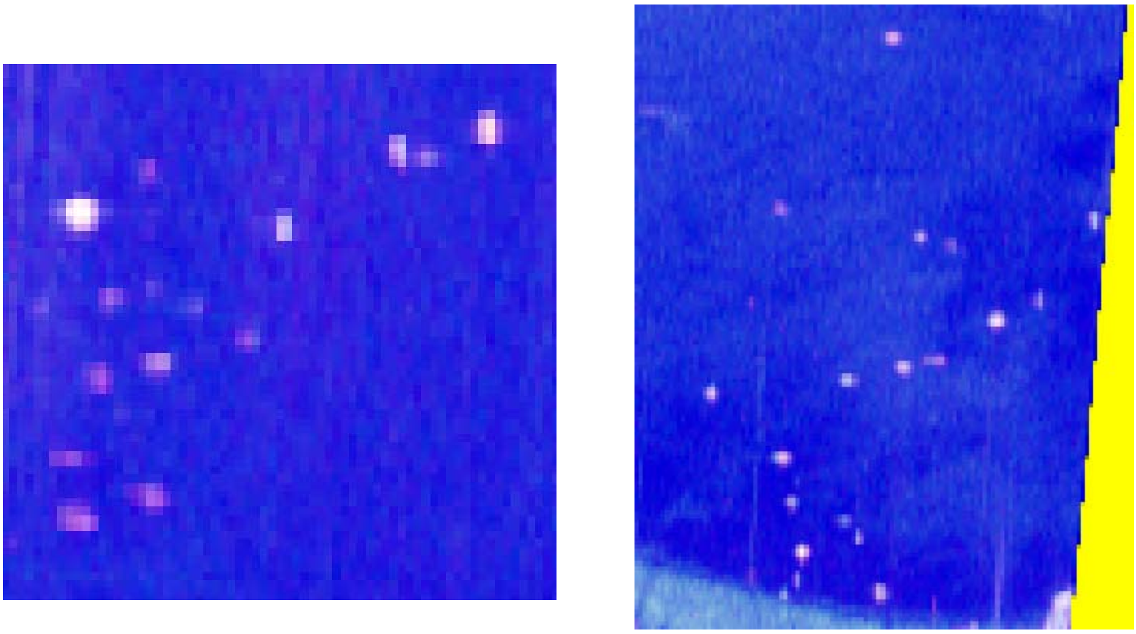

(a) Group I (b) Group II

Figure 47: Zoomed-in colour composite images showing vessels in (a) Group I and (b) Group II. The red, green and blue represent the traditional HH, VV and HV components, respectively.

To quantitatively assess different polarisation modes for target detection, Table 9 and Table 10 list the SCRs for targets in Groups I and II. In the tables, nine polarisations are studied. They are HH, VV, HV, RR, RL, slant 45^o co-polarisation and slant 45^o cross-polarisation as well as the polarisation decomposed odd and double bounce components. These SCRs are plotted in Figure 48 and Figure 49 for a visual evaluation.

Table 9: Signal-to–clutter ratios in dB for vessels in Group I.

Polarisation	Vessel No	HH	VV	HV	RR	RL	Slant 45^o	X-slant 45^o	OB	DB
Signal-to- clutter ratio (dB)	1	23.73	18.64	8.27	21.46	21.06	20.09	22.72	21.92	23.23
	2	16.39	13.69	11.45	15.79	10.94	9.61	17.97	8.91	18.21
	3	17.83	14.49	11.98	17.69	11.68	12.26	19.29	10.98	19.59
	4	9.03	1.45	1.38	7.02	5.35	5.29	7.89	6.18	8.48
	5	29.61	25.77	18.50	29.46	21.73	21.08	31.20	21.95	31.55
	6	29.61	25.77	18.50	29.46	21.73	21.08	31.20	21.95	31.55
	7	9.25	3.41	2.99	6.90	6.28	5.25	8.17	6.62	8.65
	8	3.54	2.82	1.92	3.47	2.64	2.08	4.05	1.67	4.05
	9	2.65	0.92	1.83	1.50	2.21	3.51	1.53	2.94	1.81
	10	10.38	4.34	4.45	7.39	6.64	5.97	9.81	7.45	10.32
	11	14.74	9.30	5.17	12.83	10.93	9.32	14.43	11.72	14.91
	12	12.73	3.38	5.43	10.51	9.00	9.91	11.18	9.83	11.85
	13	12.67	4.61	5.64	11.53	7.66	7.94	12.22	8.39	12.77
	14	9.63	2.38	1.28	4.16	8.18	7.41	5.59	9.08	6.50
	15	14.73	5.88	5.33	12.08	11.44	11.33	12.91	12.29	13.59

Table 10: Signal-to-clutter ratios in dB for vessels in Group II.

Polarisation	Vessel No	HH	VV	HV	RR	RL	Slant 45o	X-slant 45o	OB	DB
Signal-to- clutter ratio (dB)	1	20.71	9.65	11.40	20.23	12.41	12.53	20.96	20.50	23.10
	2	11.04	3.65	10.39	12.95	3.17	4.33	12.54	10.19	14.41
	3	14.06	8.10	9.01	14.45	8.92	9.42	14.34	16.94	16.16
	4	6.32	0.80	3.08	5.67	1.33	1.05	6.84	7.53	8.57
	5	12.94	11.24	15.86	17.03	9.07	10.18	16.61	10.23	17.98
	6	9.91	5.09	11.19	12.56	4.16	6.17	11.83	7.99	13.46
	7	22.99	15.66	17.90	23.76	15.43	15.38	24.36	22.95	26.20
	8	12.95	4.09	7.98	13.67	5.45	5.74	13.50	13.70	15.45
	9	18.16	11.75	12.45	20.20	4.66	5.99	21.44	1.55	23.19
	10	14.15	10.97	11.94	17.28	6.84	8.27	18.17	2.84	19.70
	11	18.93	10.67	14.10	19.27	11.54	11.61	19.69	19.76	21.60
	12	20.57	11.07	11.74	21.72	9.42	9.64	22.36	16.93	24.24
	13	22.54	16.54	10.73	23.81	14.14	14.00	25.04	17.31	26.71
	14	10.84	6.41	7.25	12.84	5.65	6.73	12.65	9.23	14.15
	15	17.83	10.38	7.00	18.96	8.11	7.74	20.02	16.12	21.80

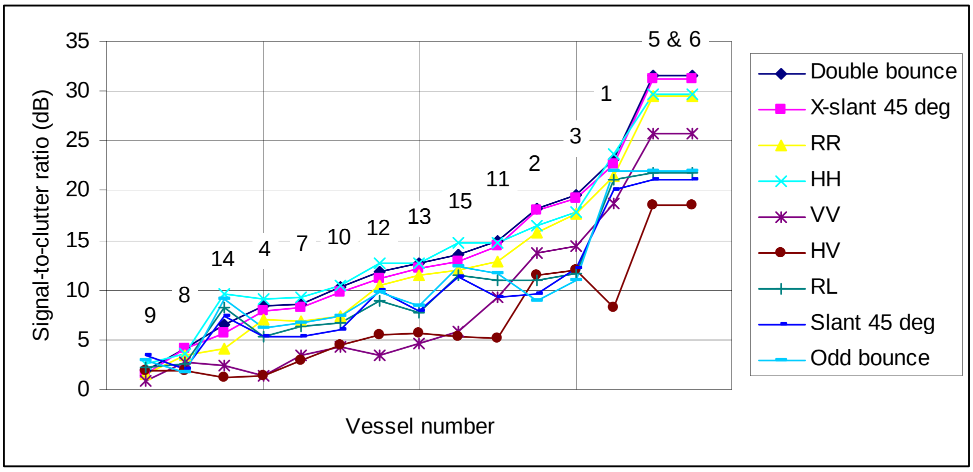

Figure 48: Signal-to-clutter ratios for vessels in Group I.

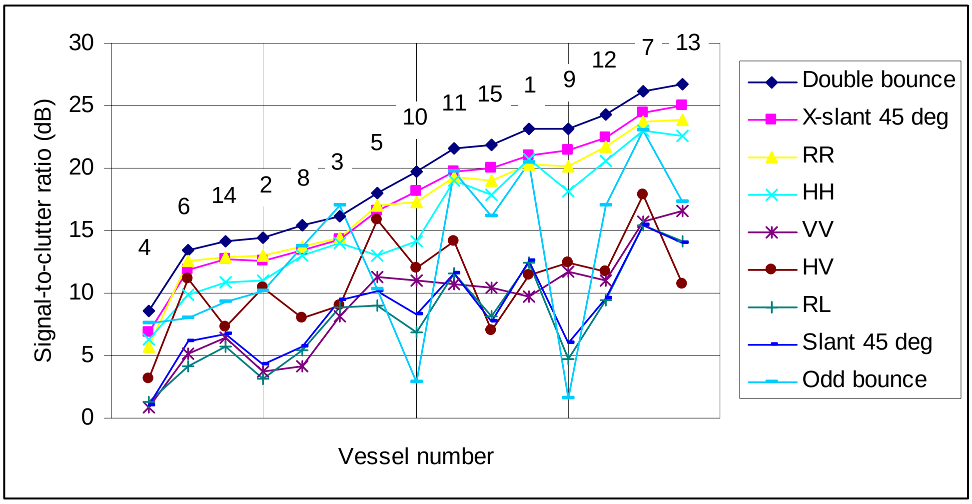

Figure 49: Signal-to-clutter ratios for vessels in Group II.

It is seen from these figures that in terms of SCR, statistically, these nine polarisations can be divided into two groups. The first group includes the double bounce, slant 45^{o} cross-polarisation, RR and HH. The remaining polarisations are in the second group and their performance is not as good as the first group. Overall the double bounce delivers the best SCR, followed by the slant 45^{o} cross-polarisation. The RR and HH perform about the same. The reasons are not difficult to find. The decomposition works like filters that filter different scatterers into different components. Sea clutter dominated by the Bragg scattering has little component in the double bounce that, on the other hand, dominates in backscatter of vessels. In the end the component of double bounce enhances the SCR for the targets. According to Table 5, slant 45^{o} cross-polarisation, RR, and HH suppress the Bragg scattering component to nearly the same level without attenuation of the double bounce scattering, therefore, they also approximately perform equally well. The remaining five polarisations either have no suppression of Bragg scattering, such as the VV polarisation, or greatly suppress the double bounce component, such as the HV, RL, slant 45^{o} co-polarisation and the decomposed single bounce. As a result, their SCRs are not as good as the first four polarisations.

5. Conclusions

This report is a continuation of the analysis of X-band polarimetric sea clutter with high resolution and high grazing angle collected by the Ingara airborne radar system in 2004. The report first focused on the correlations in both the range direction (the fast-time domain — primarily spatial correlation) and the azimuthal direction (the slow-time domain — primarily temporal correlation). Both the correlation length in range and the correlation time in azimuth are found to be shorter than those reported in the literature. This however may be attributed to the experimental conditions including high versus low grazing angles and flying versus stationary radar platforms. The analysis of the long-term correlations is interesting and promising. It seems that the wavelengths of wind waves and swells are retrievable from the range correlation whereas the periods of the wind waves and swells are also recoverable from the azimuthal correlation.

The correlation between the HH and VV sea clutter data is low. A CA-CFAR processor applying a logical 'and' to the HH and VV sea clutter data would therefore increase the SCR. This is equivalent to the use of the incoherent integration of multi-pulse data to enhance clutter suppression and improve target detection.

Analysis of the polarimetric behaviour of sea clutter has suggested that at high grazing angles, the HH radar outperforms the VV radar in terms of target detection. In the region of $0 < cdf < 0.9999$, the HH sea clutter is about 4 to 8dB lower than the VV sea clutter. The Cloude-Pottier Entropy-Alpha decomposition shows that the distribution of high grazing angle sea clutter spreads and covers a large portion of the feasible decomposition area indicating that scattering mechanisms of sea clutter are complex and multiple. It is also shown that the scattering mechanisms of the vertically polarised sea spikes that cause false alarms are simpler and often only one scattering mechanism is dominant in the VV spikes, whereas the HH spikes are more complex and often more than one scatterer contributes to the HH spikes.

The polarimetric analysis for target detection has also been discussed. To support the study, a C-band polarimetric SAR dataset collected by the NASA/JPL AirSAR system has been re-examined. Three groups of anchored small wooden vessels used as test targets were imaged in the dataset. A polarimetric decomposition technique has been applied to the dataset. The results indicate that while the sea surface is dominated by the Bragg scattering, the test vessels as well as urban areas are dominated by the double and odd bounce scattering mechanisms. Quantitative analysis indicates that the best polarisations, in terms of detecting targets on the sea surface, include double bounce, cross-slant 45^{o}, RR and HH polarisations. The other polarisations such as odd bounce, VV, HV, RL, co-45^{o} polarisations are not as good as the former set.

DSTO has recently collected another X-band dataset from the Darwin area using the Ingara system. Completed in May 2006, this trial also included small vessels on the sea surface. A similar analysis is planned to be carried out and reported in the near future.

6. Acknowledgement

ISRD of DSTO provided the sea clutter data for this study. In particular the support from Mr R Smith, Mr M Preiss and Dr D Crisp is acknowledged. JPL provided the AirSAR dataset.

Comments made by Dr B Haywood and Dr A Shaw are also acknowledged. Mr P Lawrence officially reviewed the manuscript, and his constructive comments are also acknowledged.

7. References

Billingsley, J B, *Low-Angle Land Clutter Measurements and Empirical Models*, William Andrew Publishing, 2002.

Chan, H C, “Radar sea clutter at low grazing angles,” *IEE Proceedings*, Vol 137, Pt F, no. 2, pp. 102-112, 1990.

Cloude, S, and Pottier, E, “An entropy based classification scheme for land applications of polarimetric SAR”, *IEEE Trans on Geoscience and Remote Sensing*, vol. 35, pp. 68-78, 1997.

Cohen, L, *Time-Frequency Analysis*, Prentice Hall, 1995,

Crisp, D J, Stacy, N J S, and Goh, A S, “Ingara medium-high incidence angle polarimetric sea clutter measurements and analysis”, Technical Report, *DSTO-TR-1818*, Defence Science Technology Organisation, 2006.

Dong, Y and Forster, B C, “Detection of wooden vessels using SAR data,” Technical Report to the Land, Space and Optoelectronics Division, and the Microwave Radar Division, DSTO, 1998.

Dong, Y, Forster, B C, and Ticehurst, C, “A new decomposition of radar polarization signatures”, *IEEE Trans on Geoscience and Remote Sensing*, vol. 36, no. 3, pp. 933-939, 1998.

Dong, Y, “Distribution of X-band high resolution and high grazing angle sea clutter”, Research Report, DSTO-RR-0316.

Elachi, C, *Introduction to the Physics and Techniques of Remote Sensing*, Wiley, NY, 1987.

Farina, A, Gini, F, and Verrazzani, L, “High resolution sea clutter data: statistical analysis of recorded live data”, *IEE Proc~ Radar, Sonar and Navig*, Vol 144, no. 3, pp. 121-130, 1997.

Holliday, D, Deraad, Jr., L L, and St-Cyr, G J, "Forward-backward method for scattering from imperfect conductors", *IEEE Trans on Antennas and Propagation*, vol. 46, no. 1, pp. 101-107, 1988.

Lawson, C L, and Hanson, R J, *Solving Least Squares Problems*, Prentice-Hall Inc., Englewood Cliffs, NJ, 1974.

Lee, P H Y, Barter, J D, Caponi, E, Caponi, M, Hindman, C L, Lake, B M, and Rungaldier, H, "Wind-speed dependence of small-grazing-angle microwave backscatter from sea surfaces", *IEEE Trans on Antennas and Propagation*, vol. 44, no. 3, pp. 333-340, 1996.

Lombardo, P, and Oliver, C J, "Estimating the correlation properties of K distributed SAR clutter", *IEE Proc.~ Radar, Sonar and Navigation*, vol. 142, no. 4, pp. 167-178, 1995.

Long, M W, *Radar Reflectivity of Land and Sea*, 3rd edition, Artech House, 2001.

Morris, J, "Polarimetric properties of radar echoes from features on ocean surface", PhD thesis, the University of Adelaide, 2004.

Pond, S, and Pickard, G L, *Introductory Dynamic Oceanography*, Pergamon Press, 1978.

Porat B, *A Course in Digital Signal Processing*, John Wiley & Sons, Inc, 1997.

Posner, F, "Spiky sea clutter at high range resolutions and very low grazing angles", *IEEE Trans on Aerospace and Electronic Systems*, vol. 38, no. 1, pp. 58-73, 2002.

Proakis, J G, and Manolakis, D G, *Digital Signal Processing*, 3rd edition, Prentice-Hall Inc, 1996.

Sarabandi, K, "Derivation of phase statistics from the Mueller matrix", *Radio Science*, vol. 27, pp. 553-560, 1992.

Sekine, M and Mao, Y, *Weibull Radar Clutter*, Peter Peregrinus Ltd, 1990.

Stehwien, W, "Statistics and correlation properties of high resolution X-band sea clutter", *Proceedings of the 1994 IEEE National Radar Conference*, pp. 46-51.

Trizna, D B, "Statistics of low grazing angle radar sea clutter for moderate and fully developed ocean waves", *IEEE Trans on Antennas and Propagations*, vol. 39, no. 12, pp. 1681, 1690, 1991.

Ulaby, F T, and Elachi, C, *Radar Polarimetry for Geoscience Applications*, Artech House Inc., Boston, 1990.

Ward, K D, Baker, C J, and Watts, S, "Maritime surveillance radar – Part I: Radar scattering from the ocean surface", *IEE Proc. Part F,* vol. 137, no. 2, pp. 51-62, 1990.

Ward, K D, Tough, R J A, and Watts, S, *Sea Clutter: Scattering the K Distribution and Radar Performance*, Institute of Engineering Technology, 2006.

Watts, S, "Radar detection prediction in sea clutter using the compound K distribution model", *IEE Proceedings, Pt F,* vol. 32, no. 7, pp. 613-620, 1985.

Watts, S, "Cell-averaging CFAR gain in spatially correlated K-distributed clutter", *IEE Proc~ Radar, Sonar and Navig*, vol. 143, no. 5, pp. 321-327, 1996a.

Watts, S, "Optimum radar polarisation for target detection in sea clutter", IEE Colloquium, *Polarisation in Radar*, 22 March 1996b.

DEFENCE SCIENCE AND TECHNOLOGY ORGANISATION
DOCUMENT CONTROL DATA

1. PRIVACY MARKING/CAVEAT (OF DOCUMENT)

2. TITLE

High Grazing Angle and High Resolution Sea Clutter: Correlation and Polarisation Analyses

3. SECURITY CLASSIFICATION (FOR UNCLASSIFIED REPORTS THAT ARE LIMITED RELEASE USE (L) NEXT TO DOCUMENT CLASSIFICATION)

Document	(U)
Title	(U)
Abstract	(U)

4. AUTHOR(S)

Yunhan Dong

5. CORPORATE AUTHOR

Defence Science and technology Organisation
PO Box 1500
Edinburgh South Australia 5111 Australia

6a. DSTO NUMBER	6b. AR NUMBER	6c. TYPE OF REPORT	7. DOCUMENT DATE
DSTO-TR-1972	AR-013-872	Technical Report	March 2007

8. FILE NUMBER	9. TASK NUMBER	10. TASK SPONSOR	11. NO. OF PAGES	12. NO. OF REFERENCES
2006/1115618	AIR 05/263	DGAD	58	30

13. URL on the World Wide Web

http://www.dsto.defence.gov.au/corporate/reports/DSTO-TR-1972.pdf

14. RELEASE AUTHORITY

Chief, Electronic Warfare and Radar Division

15. SECONDARY RELEASE STATEMENT OF THIS DOCUMENT

Approved for public release

OVERSEAS ENQUIRIES OUTSIDE STATED LIMITATIONS SHOULD BE REFERRED THROUGH DOCUMENT EXCHANGE, PO BOX 1500, EDINBURGH, SA 5111

16. DELIBERATE ANNOUNCEMENT

No Limitations

17. CITATION IN OTHER DOCUMENTS Yes

18. DSTO Research Library Thesaurus

Sea clutter
Scattering
Radar
Performance

19. ABSTRACT

Spatial and temporal correlations of high grazing angle high resolution sea clutter collected by the DSTO Ingara polarimetric X-band system are studied. It seems that wavelengths of wind waves and swells are retrievable from the range correlation whereas the periods of the waves and swells are recoverable from the azimuthal correlation. The polarimetric behaviour of sea clutter is also studied, and it is found that the Bragg scattering is the dominant scattering mechanism of the sea clutter. Quantitative analysis indicates that the best polarisations in terms of detecting small targets on the sea surface include double bounce, cross-slant-45-degree, RR and HH polarisations.